Remote Sensing of Environment 172 (2016) 109–125

Contents lists available at ScienceDirect

Remote Sensing of Environment

journal homepage: www.elsevier.com/locate/rse

Long-term and fine-scale satellite monitoring of the urban heat island effect by the fusion of multi-temporal and multi-sensor remote sensed data: A 26-year case study of the city of Wuhan in China

Huanfeng Shen [a,*], Liwen Huang [a], Liangpei Zhang [b], Penghai Wu [c], Chao Zeng [b]

[a] *School of Resource and Environmental Sciences, Wuhan University, Wuhan, Hubei 430079, China*
[b] *The State Key Laboratory of Information Engineering in Surveying, Mapping and Remote Sensing, Wuhan University, Wuhan, Hubei 430079, China*
[c] *School of Resources and Environmental Engineering, Anhui University, Hefei 230601, China*

ARTICLE INFO

Article history:
Received 23 October 2014
Received in revised form 3 November 2015
Accepted 11 November 2015
Available online xxxx

Keywords:
Surface urban heat island (SUHI) effect
Land surface temperature (LST)
Multi-temporal fusion
Multi-sensor fusion

ABSTRACT

The trade-off between the temporal and spatial resolutions, and/or the influence of cloud cover, makes it difficult to obtain continuous fine-scale satellite data for surface urban heat island (SUHI) analysis. To relieve these difficulties, this study employs multi-temporal and multi-sensor fusion methods for a long-term and fine-scale summer SUHI analysis of the city of Wuhan in China. By integrating several series of satellite images, we generated 26-year (1988 to 2013) high spatial resolution (Landsat-like) summer land surface temperature (LST) data. This series of data was then used for a qualitative and quantitative analysis of the SUHI patterns, evolution characteristics, and mechanisms. This study not only provides a generalized research framework for the long-term and fine-scale analysis of the SUHI effect, but also reveals several findings about the heat distribution and SUHI characteristics in Wuhan. Firstly, our results show that the high temperature and sub-high temperature areas were continuously concentrated from rural to urban areas, but the high temperature area within the old city zones showed an obvious decreasing tendency. Secondly, a more important finding is that the SUHI intensity first increased and then decreased over the 26 years. The maximum temperature difference between the city zone and the rural area was in 2003 (7.19 K for the old city zone, and 4.65 K for the area within the third ring road). Finally, we confirm that the relationships between heat distribution and land cover (especially vegetation and impervious surfaces) were interannually stable, and that the influences of industry, businesses, and residential districts on the SUHI effect were in descending order in Wuhan.

1. Introduction

More than 50% of the human population lives in cities, and this proportion is projected to increase to 60% by 2030 (DESA, 2002; Zhou, Huang, & Cadenasso, 2011). Rapid urbanization results in increasing replacement of natural landscapes by impervious surfaces, which can alter the surface radiation, thermal properties, and humidity over urban areas (Wang et al., 2007). One of the environmental consequences of urbanization is the urban heat island (UHI) effect. This describes the phenomenon of higher temperatures occurring in urban areas than in the surrounding suburban/rural areas (Oke, 1982). The UHI effect can alter biodiversity (Knapp, Kühn, Stolle, & Klotz, 2010), climate (Dixon & Mote, 2003; Kalnay & Cai, 2003; Mackey, Lee, & Smith, 2012), and even air conditions (Grimm et al., 2008; Lo & Quattrochi, 2003); therefore, it can have a great influence on the quality of life and human well-being in urban areas (Harlan, Brazel, Prashad, Stefanov, & Larsen, 2006; Lafortezza, Carrus, Sanesi, & Davies, 2009; Steeneveld, Koopmans, Heusinkveld, Van Hove, & Holtslag, 2011).

The UHI effect can be evaluated by both air temperature measurements and satellite LST measurements. The measurement of air temperature is performed either on a traverse through a city or by comparing temperatures from point measurements (Schwarz, Lautenbach, & Seppelt, 2011). In general, air temperature UHI measurements have a high temporal resolution with extensive time coverage, and can effectively describe the temporal variation of the UHI effect (Li, Zhou, & Ouyang, 2013). However, because of the sparse distribution of observation stations, a spatially continuous analysis is often difficult. To solve these problems, many studies of the UHI effect have been based on land surface temperature (LST) measurements from remote sensors. The remotely sensed UHI has been termed the surface urban heat island (SUHI) effect (Streutker, 2002; Voogt & Oke, 2003). One important advantage of using remotely sensed data is the wall-to-wall continuous coverage of the urban area (Li et al., 2011). Therefore, LST derived from thermal infrared remote sensors has become one of the most commonly used indicators for heat island analysis.

---

* Corresponding author.
E-mail address: shenhf@whu.edu.cn (H. Shen).

http://dx.doi.org/10.1016/j.rse.2015.11.005

Numerous studies of the SUHI effect have been carried out using large-scale satellite LST data sets, such as the AVHRR data of the NOAA satellites (Dousset & Gourmelon, 2003; Streutker, 2002, 2003) and the MODIS data of the Terra/Aqua satellites (Imhoff, Zhang, Wolfe, & Bounoua, 2010; Rajasekar & Weng, 2009b). Using MODIS data, a comparative SUHI analysis can also be implemented between daytime and nighttime (Cui & De Foy, 2012; Quan et al., 2014). However, these data are only suitable for coarse-scale urban temperature mapping with about a 1-km spatial resolution, and it has been proved that a spatial resolution of about 50 m is needed to properly estimate the SUHI effect at a district level (Sobrino, Oltra-Carrió, Sòria, Bianchi, & Paganini, 2012). Fortunately, a number of satellite systems can retrieve thermal infrared LST information with a relatively fine spatial resolution. For example, the spatial resolution of the TM/ETM+/TIRS sensors onboard the Landsat-5–8 satellites is 60 m to 120 m. Spatially fine analyses have been achieved by the use of this type of data, such as the spatio-temporal evolution of the SUHI effect (Cai, Du, & Xue, 2011; Li, Wang, Wang, Ma, & Zhang, 2009; Li, Zhang, & Kainz, 2012), as well as its relationship with vegetation (Chen, Zhao, Li, & Yin, 2006; Weng, Lu, & Schubring, 2004), impervious surfaces (Li et al., 2011; Yuan & Bauer, 2007), and other factors (Mackey et al., 2012; Zhang & Wang, 2008). Some researchers have also studied how urbanization and land use and land cover (LULC) affect the SUHI effect (Aniello, Morgan, Busbey, & Newland, 1995; Rajasekar & Weng, 2009a; Weng, 2003). In recent years, the Landsat series of satellites has been the foremost data source for fine-scale SUHI analysis, although the Landsat satellites do not acquire nighttime images.

Accurate time series data are very important for the monitoring of SUHI growth (Streutker, 2003). Long-term remotely sensed data can help us to more intuitively understand the evolution mechanism of the SUHI effect and its relationship with LULC and/or climate change (Li et al., 2012), and can therefore help decision-makers develop and execute rational land-use policies (Zhang et al., 2013). However, due to the limited spatial coverage, poor temporal resolution, and the influence of cloud cover, it is often difficult to obtain a long-term data sequence at a finer scale. For instance, although the Landsat satellites have a revisit cycle of 16 days, the effects of clouds, as well as stripe gaps (Landsat-7), can lead to there being no available data over a period of several months. It is also well known that the difference in the SUHI patterns of different seasons can be quite obvious (Li et al., 2012). Therefore, an LST data sequence for long-term SUHI analysis should be obtained in the same season, which further increases the difficulties of image acquisition. This contradiction between supply and demand for satellite data is a very common problem in SUHI research. As a result, most of the existing studies of long-term SUHI patterns have had to use only a few representative remotely sensed images (Li et al., 2012; Zhang et al., 2013). The use of discontinuous data can result in great uncertainty when drawing conclusions. How to realize a temporally continuous fine-scale view of the SUHI effect is therefore an open and significant issue.

The main objectives of this paper are: 1) to solve the spatio-temporal discontinuity of remotely sensed LST for a summer SUHI analysis; and 2) to provide a long-term (26-year) and fine-scale (Landsat-like) case study of the city of Wuhan in China. Multi-temporal and multi-sensor fusion methods were employed to obtain spatially continuous summer LST data from 1988 to 2013 by integrating the observations of NOAA-AVHRR, Terra-MODIS, Landsat-5 TM, Landsat-7 ETM+, and Landsat-8 OLI/TIRS. Based on the long-term and fine-scale data, a SUHI evolution analysis of Wuhan was carried out, and a number of important findings were revealed.

2. Methods

2.1. Study area

The Wuhan metropolis was chosen as the study area in this research. Wuhan is located between 113°41′–115°05′ E and 29°58′–31°22′ N, having a total area of 8494.41 km^2 and a population of about 10.02 million. Since China's "Open and Reform Policy" started at the end of the 1970s, Wuhan has experienced rapid urbanization over the last three decades. As the capital of Hubei province, it has been recognized as the economic, educational, and transportation center of central China (as shown in Fig. 1 (a) and (b)). The confluence of the middle reaches of the Yangtze River and Han River divides the metropolitan area into three parts, namely Wuchang, Hankou, and Hanyang (as shown in Fig. 1 (c)). In order to avoid image mosaicing and the associated problems, a single standard scene of Landsat data covering about 80% of Wuhan was used in this research. From Fig. 1 (c), it can be seen that the Wuhan metropolis is located at the center of this study area. The study area can therefore be considered as being representative of the whole of the city of Wuhan.

Wuhan has a subtropical monsoon climate, with the mean annual temperature ranging from 288.95 K to 290.65 K. It is noteworthy that Wuhan is regarded as one of the hottest "stove cities" in China (Han, Li, & Zheng, 2009; Qian et al., 2007; Su, Gu, & Yang, 2010), especially in summer, and the temperature at night is the highest of all the large cities in China. Research into the summer SUHI mechanism is therefore of special significance. In this study, we obtained daily highest air temperatures from 2001 to 2010 from meteorological data, and then calculated the 10-year average highest temperatures of each day (see Fig. 2). After analyzing these data, and considering the data availability, we considered the 100 hottest days to be the "ideal date range", which was from the middle of June to the middle of September (between the thick lines in Fig. 2). All the observed or fused LST data used for the SUHI analysis were from this ideal range, with the exception of three LSTs which were observed close to this range in September, as illustrated in Fig. 2 by the thin lines. It should be noted that although these three exceptions were out of the ideal summer period, the air temperatures were still quite high (301.35 K, 303.95 K, and 308.85 K); therefore, they had little effect on the subsequent analysis.

2.2. The satellite data

We first collected the available Landsat-5, Landsat-7, and Landsat-8 images, which were acquired in the date range of Fig. 2 in the years from 1988 to 2013. Due to the effects of clouds and gaps, the Landsat images were only available for a total of 10 years. To make up for the data deficiency and to obtain continuous 26-year data, some Landsat (out of the date range), MODIS, and AVHRR data (within the date range and/or out of the date range) were collected for the multi-temporal and multi-sensor fusion. By the data fusion, continuous fine-scale LSTs within the ideal data range could be obtained. In summary, the data used in this study are listed in Table 1.

For MODIS, the MOD11A1 LST product was directly used. For the other sensor data, the LSTs were retrieved using the existing standard algorithms described in the next section. The thermal infrared bands of Landsat-5 TM, Landsat-7 ETM+, Landsat-8 TIRS, MODIS, and AVHRR have spatial resolutions of 120 m, 60 m, 100 m, 1 km, and 1.1 km, respectively. Since the downloaded Landsat data had been resampled to a 30-m resolution, the analysis was performed at this scale. In addition to the thermal infrared bands and the LST products, the reflective bands were also needed to compute the normalized difference vegetation index (NDVI), the impervious surface fraction (ISF), and the vegetation fraction (VF) for the correlation analysis. All the satellite data were rectified to the Universal Transverse Mercator (UTM) projection system (Spheroid WGS84, Datum WGS84, and Zone 49).

2.3. LST retrieval methods

2.3.1. LST retrieval from Landsat images

There have been several algorithms developed for the retrieval of LST from Landsat images, including the mono-window algorithm (Qin, Karnieli, & Berliner, 2001), the single-channel algorithm (Jiménez-

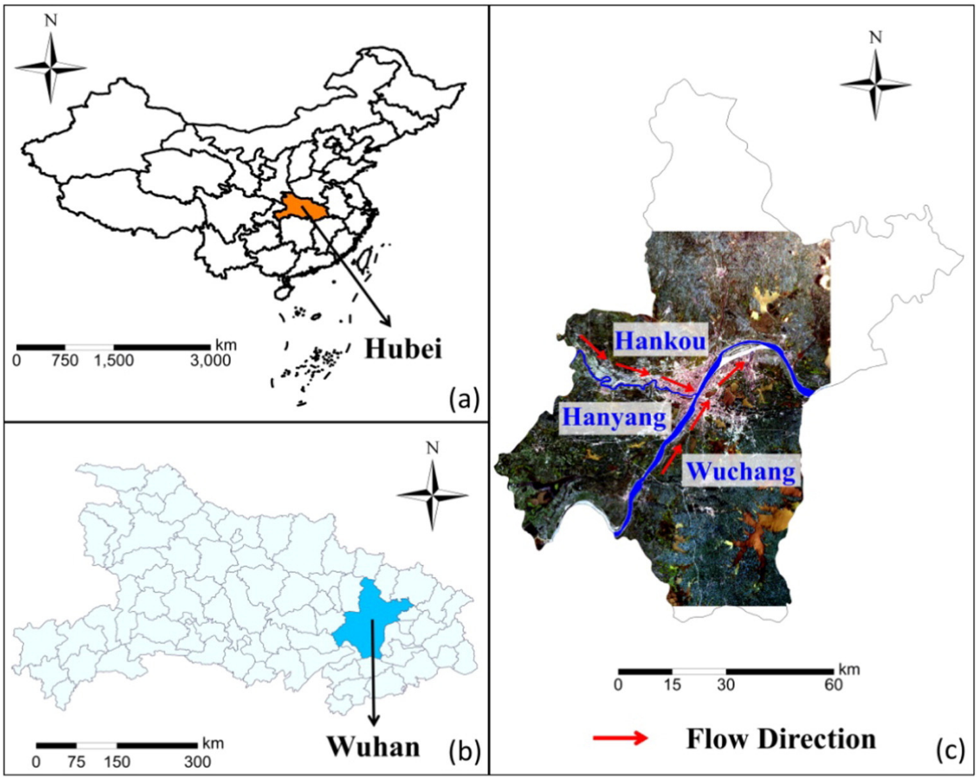

Fig. 1. The study area. (a) The location of Hubei province in China. (b) The administrative boundary of Wuhan in Hubei province. (c) Landsat-7 ETM+ image of Wuhan on 22 July 2001 (covering about 80% of Wuhan). The thin and thick blue lines are respectively used to indicate the Han River and Yangtze River, which divide Wuhan into three parts: Hankou, Hanyang, and Wuchang. (For interpretation of the references to color in this figure legend, the reader is referred to the web version of this article.)

Muñoz & Sobrino, 2003), and the radiative transfer equation algorithm (Sobrino, Jiménez-Muñoz, & Paolini, 2004). However, it is difficult to acquire near-real-time atmospheric profile data for when the satellites pass over the study area, which is necessary when utilizing these methods. Therefore, like many other UHI studies (Li et al., 2009, 2011, 2012; Weng, 2003), we chose a method in which only the TOA spectral radiance and the NDVI are necessary. The parameter information in the header file can be easily used to obtain the TOA spectral radiance and reflectance of the Landsat TM/ETM (Chander, Markham, & Helder, 2009; Li et al., 2011) and Landsat-8 OLI/TIRS data (http://landsat.usgs.gov/Landsat8_Using_Product.php).

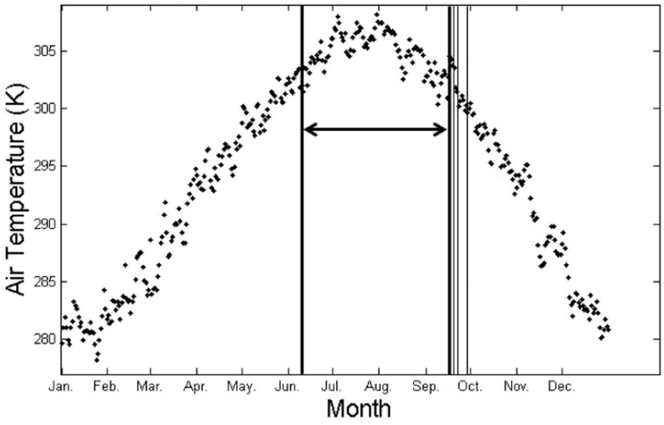

Fig. 2. The date range of the remotely sensed LST data. The dots represent the daily maximum temperatures averaged from 2001 to 2010, the interval between the two thick lines is the ideal data range, and the dates corresponding to the three thin lines represent the exceptions out of the ideal range.

Adopting the conversion formula, the spectral radiance values of the Landsat thermal infrared bands were converted to at-sensor brightness temperatures, under the assumption of uniform emissivity (Chander et al., 2009):

$$T_{sensor} = \frac{K_2}{\ln(K_1/L_\lambda + 1)} \tag{1}$$

where T_{sensor} is the effective at-sensor brightness temperature in kelvin (K), L_λ is the TOA spectral radiance in $W/(m^2 sr\mu m)$, and K_1 and K_2 are the calibration constants. For Landsat-5 TM, K_1 is 607.76 $W/(m^2 sr\mu m)$ and K_2 is 1260.56 K; for Landsat-7 ETM+, K_1 is 666.09 $W/(m^2 sr\mu m)$ and K_2 is 1282.71 K; and for Landsat-8 TIRS, K_1 is 774.89 $W/(m^2 sr\mu m)$ and K_2 is 1321.08 K for band 10 (http://landsat.usgs.gov/Landsat8_Using_Product.php).

The T_{sensor} values obtained above were referenced to a black body, which is quite different to the properties of real objects. Therefore, it

Table 1
The satellite data used in the study.

Sensor	Date				
Landsat-5 TM	1988-08-11	1990-09-02	1991-07-19	1993-08-09	1994-09-29
	1995-08-31	2000-09-13	2003-04-15	2004-02-13	2005-04-20
	2006-11-01	2008-04-28	2009-09-06	2010-12-30	2011-06-08
Landsat-7 ETM+	2001-07-22	2002-03-19	2002-07-09	2003-07-28	2004-09-16
	2005-07-17	2006-03-30	2007-01-28	2008-05-06	2010-09-17
	2011-03-12	2011-12-09	2012-03-14		
Landsat-8 OLI/TIRS	2013-06-13				
MODIS	2002-03-19	2004-07-23	2004-09-16	2006-03-30	2006-08-14
	2007-01-28	2007-07-28	2008-05-06	2008-07-27	2011-03-12
	2011-07-02	2012-03-14	2012-09-15		
AVHRR	1989-07-15	1992-07-29	1996-07-24	1997-08-21	1998-09-18
	1999-06-18				

was necessary to correct the spectral emissivity, and the LST based on satellite brightness temperature (T_{sensor}) was computed by the following equation (Artis & Carnahan, 1982):

$$LST = \frac{T_{sensor}}{1 + (\lambda \times T_{sensor}/\alpha)\ \ln(\varepsilon)} \tag{2}$$

where LST is the LST in K; T_{sensor} is the black body temperature, and also the satellite brightness temperature in K; λ is the wavelength of the emitted radiance in meters;$\alpha = 1.438 \times 10^{-2}$mK; and ε is the surface emissivity.

For ε, water (NDVI < 0) was assigned a value of 0.9925, urban impervious areas and bare soil ($0 = <$NDVI < 0.15) were assigned a value of 0.923 (Xie, Zhou, Teng, & Wang, 2012), and vegetation (NDVI > 0.727) was assigned a value of 0.986 (Valor & Caselles, 1996). Otherwise, there was a modeling relationship with the NDVI values through the following equation (Van de Griend & Owe, 1993):

$$\varepsilon = 1.0094 + 0.047\ \ln(\text{NDVI}). \tag{3}$$

Considering that the atmospheric environment is different between urban and rural areas (Kuttler, Weber, Schonnefeld, & Hesselschwerdt, 2007; Sisterson and Dirks, 1967; Tapper, 1990), and in order to obtain accurate NDVI data, atmospheric correction is necessary to convert the TOA reflectance to surface reflectance. The 6S and MODTRAN models are two commonly employed methods (Adler-Golden et al., 1999; Masek et al., 2006). In this study, we used the MODTRAN-based FLAASH (Fast Line-of-sight Atmospheric Analysis of Spectral Hypercubes) model embedded in ENVI software for the atmospheric correction.

2.3.2. LST retrieval from MODIS and AVHRR images

In this study, the MOD11A1 LST product was directly utilized. This LST product is produced by the MODIS Science Team as a daily 1-km global land product, and can be obtained from the download URL (http://ladsweb.nascom.nasa.gov/data/search.html). It is retrieved with a generalized split-window algorithm (Wan, Zhang, Zhang, & Li, 2004), and includes derivative products at lower temporal frequencies and spatial resolutions. The MODIS LST accuracy is better than 1 K in the range from 263.15 K to 323.15 K. It was validated from in situ measurement data collected in field campaigns between 2000 and 2002 (Wan et al., 2004; Wu, Shen, Ai, & Liu, 2013).

The Planck's function (Streutker, 2003) was employed to retrieve the brightness temperatures from the radiance of the AVHRR images. In the implementation of this algorithm, the radiance values for channel 4 (10.3–11.3 μm) and channel 5 (11.5–12.5 μm) were first calculated using the calibration coefficients contained within the ephemeris data. These radiance values were then corrected using radiance correction coefficients. Following this, the corrected radiance (R_i) values were converted to brightness temperatures by the use of the following equation (Streutker, 2002):

$$T_i(R_i) = C_2 v_i / \ln\left(1 + \frac{C_1 v_i^3}{R_i}\right). \tag{4}$$

where $C_1 = 1.1910659 \times 10^{-5}$mWm^{-2}sr^{-1}cm^4, $C_2 = 1.438833$cmK, and v_i is the central wave number of each channel. Finally, the brightness temperature data from the split-window channels were used to calculate the surface temperature by the use of the following formula (Streutker, 2002):

$$T_{surface} = T_4 + R(T_4 - T_5) \tag{5}$$

where T_4 and T_5 are the brightness temperatures of the two channels, and $R = 1/[(\beta_4/\beta_5 - 1)] = 3.33$($\beta_4$ and β_5 are the atmospheric absorption coefficients for channels 4 and 5).

2.4. Fusion methods

2.4.1. Multi-temporal fusion method

A multi-temporal fusion method was employed to recover the information affected by fractus clouds and ETM+ gaps in the Landsat images. The primary image to be recovered was always in the ideal date range (see Fig. 2). The recovery was implemented by fusing the primary image and an auxiliary image, which may have been acquired out of the ideal date range. Therefore, the main problem was how to use the information in the auxiliary image to fill the vacant pixels in the primary image. Here, a multi-temporal linear regression method (Zeng, Shen, & Zhang, 2013) was employed. For each target pixel, the linear relationship hypothesis is represented as:

$$Y_t = a \cdot X_t + b \tag{6}$$

where Y_t and X_t are the pixels at the target location in the primary image and auxiliary image, respectively, and a and b are the regression coefficients calculated in a local search window using similar pixels. An adaptive determination procedure for the search window and similar pixels can be found in Zeng et al. (2013).

If there are N similar pixels in the search window, the regression equation can be solved by the weighted least-squares method. For convenience, the expanded form is given as (Ruppert & Wand, 1994):

$$a = \frac{\sum_{i=1}^{N} W_i\left(Y_i - \overline{Y}\right)\left(X_i - \overline{X}\right)}{\sum_{i=1}^{N} W_i\left(X_i - \overline{X}\right)^2} \tag{7}$$

$$b = \overline{Y} - a\overline{X} \tag{8}$$

where Y_i and X_i represent the pixel values of the similar pixels in the search window in the primary and auxiliary images, respectively, $\overline{Y}$ and $\overline{X}$ are their mean values, and W_i is the normalization weight of each similar pixel. Here, a higher spectral similarity and a smaller distance for a similar pixel to the target pixel is assigned a larger weight. Thus, a synthetic difference indicator can be designed as:

$$D_i = |X_i - X_t + \alpha| \cdot \left((x_i - x_t)^2 + (y_i - y_t)^2\right) \tag{9}$$

where x_i, y_i, x_t, and y_t represent the locations of the similar pixel and target pixel, and α is a small value to prevent D_i equaling zero. The weights of each similar pixel are then normalized as:

$$W_i = (1/D_i) / \sum_{i=1}^{N} (1/D_i). \tag{10}$$

After normalization, the range of weight W_i is from 0 to 1, and the sum of all the similar pixel weights is 1.

2.4.2. Multi-sensor fusion method

A multi-sensor fusion method was employed to offset the trade-off between the temporal and spatial resolutions of the different sensors. The spatial and temporal adaptive reflectance fusion model (STARFM) was utilized to fuse the Landsat and MODIS images to generate the daily reflectance data with a 30-m spatial resolution (Gao, Masek, Schwaller, & Hall, 2006). This method and the extended STARFM method have also been applied to other parameters of remote sensing data, such as the NDVI (Meng, Du, & Wu, 2013) and LST (Weng, Fu, & Gao, 2014; Wu et al., 2013). In this study, a synthesis of the original and extended STARFM was used to generate the high spatio-temporal resolution LST. This approach predicts Landsat LST values at t_2, using MODIS/AVHRR LST values at t_2, and is spatially and radiance-weighted between baseline Landsat and MODIS image data acquired at t_1. The fine-resolution LST can be calculated using:

$$F\left(x_{w/2}, y_{w/2}, t_2\right) = \sum_{i=1}^{w}\sum_{j=1}^{w} W_{ij} * \left(C\left(x_i, y_j, t_2\right) + F\left(x_i, y_j, t_1\right) - C\left(x_i, y_j, t_1\right)\right) \tag{11}$$

where F and C denote the fine-resolution and coarse-resolution LST, respectively; (x_i,y_j) denotes the pixel location; t_1 is the acquisition date; t_2 is the prediction data; w is the size of the moving window; and $(x_{w/2},y_{w/2})$ is the central pixel. W_{ij} is the spatial weighting function.

The W_{ij} value determines the degree to which similar neighboring pixels within a moving window contribute to the predicted central pixel. W_{ij} can be calculated by the following equation:

$$W_{ij} = \left(1/E_{ij}\right) / \sum_{i,j=1}^{w}\left(1/E_{ij}\right) \tag{12}$$

where E_{ij} is only related to the radiance difference and geometric distance in the moving window, for a single image pair, as the t_1 input (Hilker et al., 2009; Shen et al., 2013; Wu et al., 2013), and can be expressed as:

$$E_{ij} = Ln\left(S_{ij} * A + 1\right) * D_{ij} \tag{13}$$

where A is a scale factor, which is equal to 10,000 (Gao et al., 2006), and D_{ij} and S_{ij} represent the geometric distance and radiance difference considering the observation difference, which can be easily obtained by the method developed by Gao et al. (2006):

$$S_{ij} = \left|F\left(x_i, y_j, t\right) - C\left(x_i, y_j, t\right)\right| \tag{14}$$

$$D_{ij} = 1 + d_{ij}/B \tag{15}$$

where F and C denote the fine-resolution LST and coarse-resolution LST, respectively. B is a constant that defines the relative importance of the spatial distance to the radiance and temporal distance (Gao et al., 2006). d_{ij} denotes the spatial distance between the central predicted pixel and the surrounding similar candidate pixel. The spatial similarity is normally better for a closer pixel; thus, a closer candidate should be assigned a higher weight. d_{ij} can be expressed as:

$$d_{ij} = \sqrt{\left(x_{w/2} - x_i\right)^2 + \left(y_{w/2} - y_i\right)^2} \tag{16}$$

where $(x_{w/2},y_{w/2})$ denotes the central pixel, and (x_i,y_i) denotes the candidate pixel.

2.5. Workflow for the generation of the 26-year summer LSTs

Fig. 3 shows the flowchart for the LST generation. When the Landsat images are free of clouds and gaps, the LST can be directly retrieved from the thermal infrared bands. If the Landsat images are contaminated by gaps and/or fractus clouds, the multi-temporal fusion method is employed for gap filling and/or cloud recovery before the LST retrieval. In the case of there being no available Landsat images in the date range shown in Fig. 2, the multi-sensor fusion method is employed to predict the desired LST using a Landsat LST out of the ideal range, with the auxiliary of the corresponding MODIS and/or AVHRR LSTs. Table 2 shows the processing methods for the LST generation of the different years.

It should be noted that the Landsat and MODIS LSTs can be directly fused because the difference between the acquisition times of Terra and Landsat (e.g., 10:00 A.M. and 10:30 A.M.) is very small. However, the AVHRR acquisition time is not fixed, which makes the direct fusion of AVHRR and Landsat data unreliable. To solve this problem, we fused the AVHRR LST with a pair of Landsat and MODIS LSTs which were acquired on 19 March 2002. It is noted that this choice neglects the system difference between AVHRR and MODIS, and obtains a high-resolution LST corresponding to the AVHRR acquisition time. In order to ensure consistency over time in this long-term study, a moment matching method (Gadallah, Csillag, & Smith, 2000; Shen, Jiang, Zhang, & Zhang, 2014) was employed to adjust the LSTs in different years to have the same mean and variance. As 2001 is in the middle of these years, it was selected to be the reference data for the moment matching. Since we have a yearly continuous data sequence, a one-dimension low-pass temporal filtering could be further performed on the LST to relieve the possible uncertainties. In this study, an average filter with a window size of 3 was used.

2.6. The strategy of temperature grading

Temperature grading can generate a temperature map which can be utilized to study the evolution of the SUHI pattern (Li et al., 2012). Many researchers have used the absolute temperature grading strategy (ATGS) that divides the LST images into defined temperature ranges (Chen et al., 2006; Li et al., 2012). However, in temporal analysis of the SUHI effect, the air temperatures on the satellite imaging dates are commonly different, which can result in the serial LSTs of the same object having considerable differences, even if the object itself has not changed. Furthermore, the parameter uncertainties in LST retrieval

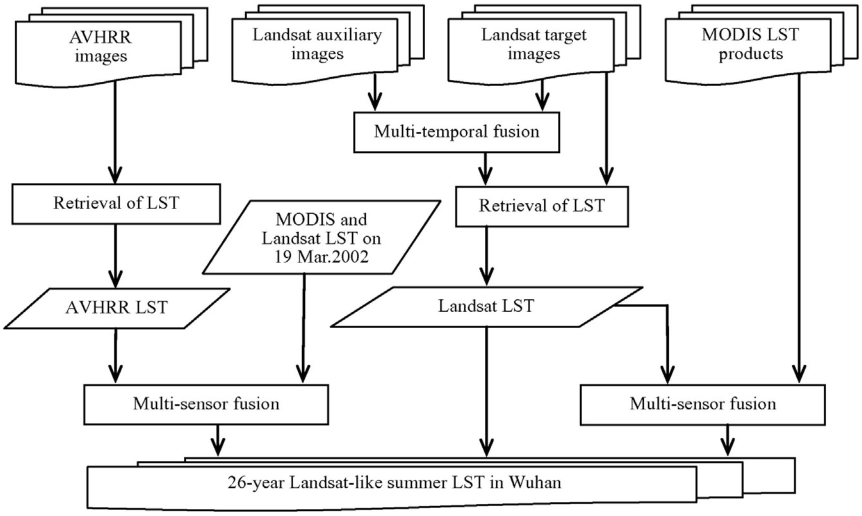

Fig. 3. The flowchart of LST production processing.

Table 2
Acquisition methods for the 26-year LSTs in Wuhan (MS: multi-sensor fusion result; MT: multi-temporal fusion result; R: retrieval from Landsat data).

Year	Method	TM/ETM+/TIRS	MODIS	AVHRR	Result
1988	Multi-temporal fusion (cloud recovery)	1988-08-11 1990-09-02			1988-08-11 (MT)
1989	Multi-sensor fusion	2002-03-19	2002-03-19	1989-07-15	1989-07-15 (MS)
1990	Retrieval from Landsat data	1990-09-02			1990-09-02 (R)
1991	Retrieval from Landsat data	1991-07-19			1991-07-19 (R)
1992	Multi-sensor fusion	2002-03-19	2002-03-19	1992-07-29	1992-07-29 (MS)
1993	Retrieval from Landsat data	1993-08-09			1993-08-09 (R)
1994	Retrieval from Landsat data	1994-09-29			1994-09-29 (R)
1995	Retrieval from Landsat data	1995-08-31			1995-08-31 (R)
1996	Multi-sensor fusion	2002-03-19	2002-03-19	1996-07-24	1996-07-24 (MS)
1997	Multi-sensor fusion	2002-03-19	2002-03-19	1997-08-21	1997-08-21 (MS)
1998	Multi-sensor fusion	2002-03-19	2002-03-19	1998-09-18	1998-09-18 (MS)
1999	Multi-sensor fusion	2002-03-19	2002-03-19	1999-06-18	1999-06-18 (MS)
2000	Retrieval from Landsat data	2000-09-13			2000-09-13 (R)
2001	Retrieval from Landsat data	2001-07-22			2001-07-22 (R)
2002	Retrieval from Landsat data	2002-07-09			2002-07-09 (R)
2003	Multi-temporal fusion (gap filling)	2003-04-15 2003-07-28			2003-07-28 (MT)
2004	Multi-temporal fusion (gap filling)	2004-02-13 2004-09-16			2004-09-16 (MT)
	Multi-sensor fusion	2004-09-16 (MT)	2004-09-16 2004-07-23		2004-07-23 (MT–MS)
2005	Multi-temporal fusion (gap filling)	2005-04-20 2005-07-17			2005-07-17 (MT)
2006	Multi-temporal fusion (gap filling)	2006-11-01 2006-03-30			2006-03-30 (MT)
	Multi-sensor fusion	2006-03-30 (MT)	2006-03-30 2006-08-14		2006-08-14 (MT–MS)
2007	Multi-temporal fusion (gap filling)	2006-11-01 2007-01-28			2007-01-28 (MT)
	Multi-sensor fusion	2007-01-28 (MT)	2007-01-28 2007-07-28		2007-07-28 (MT–MS)
2008	Multi-temporal fusion (gap filling)	2008-04-28 2008-05-06			2008-05-06 (MT)
	Multi-sensor fusion	2008-05-06 (MT)	2008-05-06 2008-07-27		2008-07-27 (MT–MS)
2009	Retrieval from Landsat data	2009-09-06			2009-09-06 (R)
2010	Multi-temporal fusion (gap filling)	2010-12-30 2010-09-17			2010-09-17 (MT)
2011	Multi-temporal fusion (gap filling)	2011-06-08 2011-03-12			2011-03-12 (MT)
	Multi-sensor fusion	2011-03-12 (MT)	2011-03-12 2011-07-02		2011-07-02 (MT–MS)
2012	Multi-temporal fusion (gap filling)	2011-12-09 2012-03-14			2012-03-14 (MT)
	Multi-sensor fusion	2012-03-14 (MT)	2012-03-14 2012-09-15		2012-09-15 (MT–MS)
2013	Retrieval from Landsat data	2013-06-13			2013-06-13 (R)

can also have some effect. These factors make it difficult to accurately analyze the changes in the SUHI effect. In order to reduce the influence of temperature fluctuations, a relative percentage temperature grading strategy (RPGS) was adopted to generate the temperature map in this study. This method utilizes the relative percentage range to divide the LST data, instead of the absolute temperature range. The threshold values were determined with reference to the class proportions in the study region. We obtained the classification map by the use of maximum likelihood supervised classification of a Landsat-7 image from 17 September 2010. The proportions of water, vegetation, soil, and buildings were 22.83%, 34.73%, 28.76%, and 13.68% in Wuhan, respectively. Guided by these class proportions, we determined five temperature grades of low, sub-low, middle, sub-high, and high, and set their temperature zones as 20%, 40%, 25%, 12.5%, and 2.5%, respectively. The percentages of the land-cover types and the temperature zones are shown in Table 3. In summary, the LST data were divided by this standard: from low to high, the LST data between 0% and 20% were defined as the low temperature zone; the data between 20% and 60% were defined as the sub-low temperature zone; the data between 60% and 85% were defined as the middle temperature zone; the data between 85% and 97.5% were defined as the sub-high temperature zone; and the data between 97.5% and 100% were defined as the high temperature zone. In this study, we were mainly concerned with the transfer tendency of the high and sub-high temperature zones, not the change in their areas. Therefore, the same grading standard was used in all the 26 years to ensure that the pixel numbers in each temperature zone did not vary. In this way, the heat transfer can be clearly observed from the time sequence data.

Table 3
The percentages of the different land-cover types and the temperature zones.

Cover		Temperature	
Type	Percentage	Zone	Percentage
Water	22.83%	Low	20%
Vegetation	34.73%	Sub-low	40%
Bare soil	28.76%	Middle	25%
Buildings	13.68%	Sub-high	12.5%
		High	2.5%

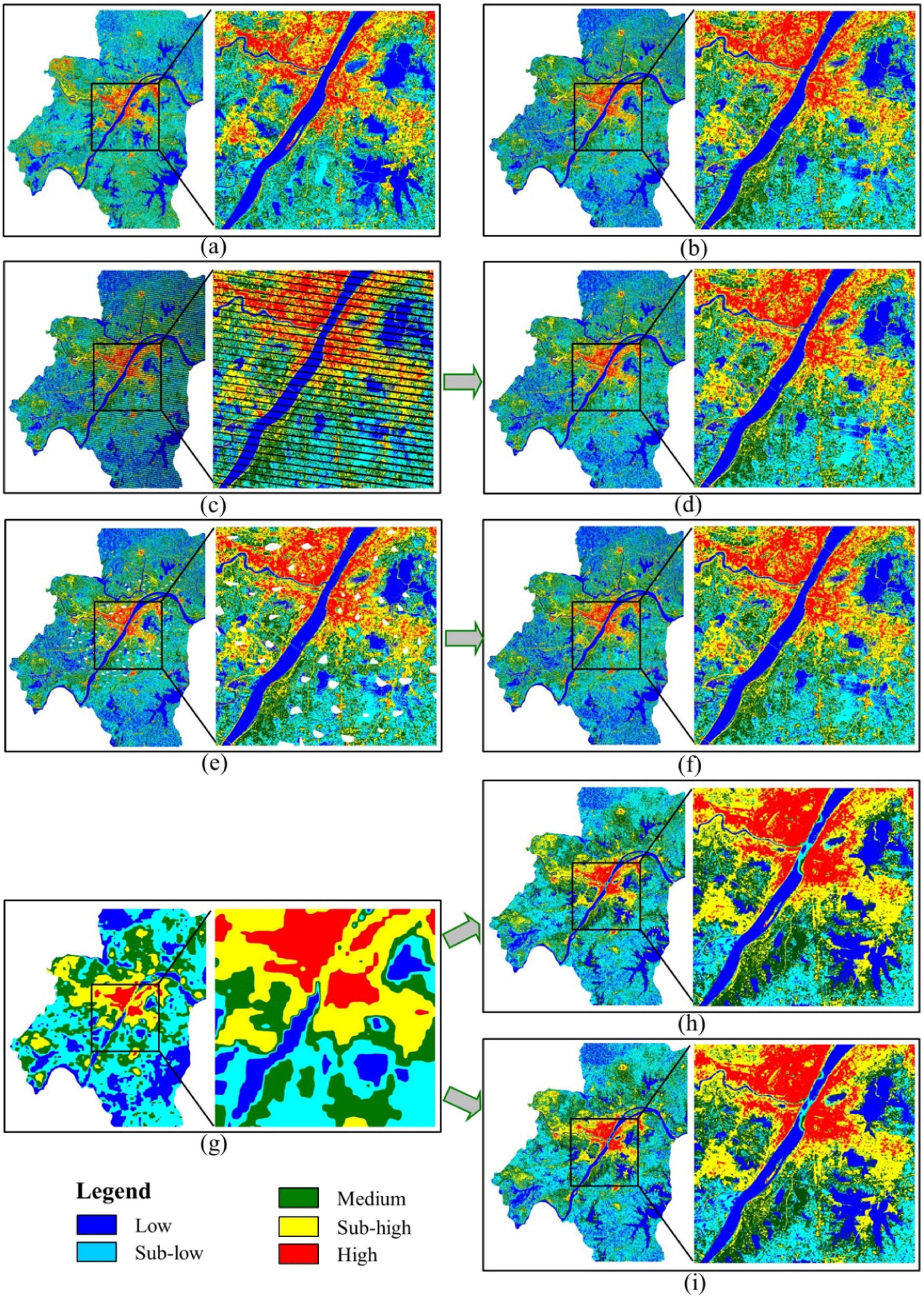

Fig. 4. Simulated validation of the fusion methods. (a) LST retrieved from the auxiliary image on 19 March 2002. (b) LST retrieved from the primary image on 9 July 2002. (c) The striped LST on 9 July 2002. (d) The multi-temporal fused LST corresponding to (c). (e) The cloud-covered LST on 9 July 2002. (f) The multi-temporal fused LST corresponding to (e). (g) The MODIS LST distribution on 9 July 2002. (h) The multi-sensor fused LST corresponding to (g). (i) The combination of multi-temporal and multi-sensor fused LST corresponding to (g).

3. Results

3.1. Simulated validation of the fusion methods

A number of simulation experiments were conducted to validate the feasibility of the multi-temporal and multi-sensor fusion methods in LST mapping. Two cloud-free Landsat-7 ETM+ images acquired on 19 March 2002 and 9 July 2002, as well as their corresponding MODIS images, were used for the simulation experiments. Fig. 4 (a) and (b) respectively show the LSTs retrieved from the ETM+ thermal infrared bands on 19 March 2002 and 9 July 2002. In the validation of the multi-temporal fusion method, the Fig. 4 (b) image was contaminated by dead pixel stripes (Fig. 4 (c)) and fractus clouds (Fig. 4 (e)), respectively. The Fig. 4 (a) image was then used as the auxiliary data to recover these simulated images by the use of the multi-temporal fusion method described in Section 2.4.1. The LSTs retrieved from the recovered images are shown in Fig. 4 (d) and (f), respectively. Here, it can be seen that the LST distributions are quite similar to the real LST shown in Fig. 4 (b). In the validation of the multi-sensor fusion method, Fig. 4 (a) was used to predict Fig. 4 (b) at the Landsat scale by the use of the multi-sensor fusion method described in Section 2.4.2, with the auxiliary data of the MODIS LSTs on these two dates. Fig. 4 (g) is the MODIS LST on the prediction date, and Fig. 4 (h) shows the fusion result. By comparing Fig. 4 (g) and (h), it can be seen the spatial resolution has been greatly improved. However, the fusion result is slightly more blurred than the real LST distribution shown in Fig. 4 (b). The main reason for this is the re-sampling process in the fusion procedure, with which the blurring problem is inevitable in regions with complex geographic features (Gao et al., 2006). Nevertheless, the spatial distribution is still quite similar to the real LST. Fig. 4 (i) is the result of the combined application of the multi-temporal and multi-sensor fusion methods, which is quite similar to Fig. 4 (h). In terms of the quantitative evaluation, the average absolute deviation (AAD) of each simulation experiment was 0.90 K, 1.20 K, 3.31 K, and 3.27 K, respectively. All these results indicate that the proposed fusion method is accurate, and we believe that it was feasible and appropriate to apply it in the SUHI analysis in this study.

3.2. Qualitative evolution analysis of urban heat distribution

Based on the LST generation method described in Section 2.5, and the temperature grading method described in Section 2.6, the 26-year Landsat-like LSTs were generated and are shown in Figs. 5 and 6, which correspond to before and after the temporal filtering, respectively. Although the LST distributions in Fig. 5 show obvious patterns of change over the 26 years, there are also some years (e.g., 1992) in which the LST distributions deviate from the overall trend. This may be due to poor data quality, extreme weather conditions, the uncertainties of the retrieval and fusion algorithms, etc. We can, however, see that the LST changes are more regular after the post-processing (as shown in Fig. 6). In summary, the proposed method can clearly reflect the evolution process of the SUHI effect.

Fig. 6 demonstrates that the LSTs in the urban areas were consistently higher than those in the surrounding rural areas. The high temperature (red) and/or sub-high temperature (yellow) zones were mainly distributed in the city proper. Moreover, their joint aggregated area in the urban regions was much lower in the early stages. This pattern of change was mainly due to the process of urbanization in Wuhan, which is quantitatively analyzed in Sections 3.3 and 3.4.

Notably, the specific distribution patterns of the high temperature and sub-high temperature zones showed dramatically different patterns of change over the 26 years. It can be seen, in the early stages, that most of the high temperature zone was concentrated in the old city zone, and the sub-high temperature zone had a relatively scattered distribution, and showed a high temperature island structure. As time passed, the high temperature zone slowly transferred outwards, and the sub-high temperature zone gradually moved towards the central part of Wuhan. In the middle stages, although the high temperature zone was still concentrated, it was more dispersed, and the heat island showed a mixture of high temperature and sub-high temperature. In recent years, most of the high temperature zone was re-concentrated into several local areas and belt structures. On the other hand, most of the sub-high temperatures were concentrated into the central urban areas of Wuhan. By 2013, the combination pattern of a global sub-high temperature heat island and local high temperature heat islands had been formed.

From the above analysis, a very interesting phenomenon is that the severest SUHI effect districts, corresponding to the high temperature zone, changed from being concentrated in the old city zone to becoming concentrated into several local clusters. In order to display this pattern of evolution at a finer scale, the analysis was further performed on the three urban areas (Fig. 1 (c)): Hankou, Hanyang, and Wuchang. In order to ensure a clearer contrast, we divided the 26-year LST data into five stages, i.e., 1988–1992, 1993–1997, 1998–2002, 2003–2007, and 2008–2013, respectively. For each stage, the average LST distribution was utilized, as shown in Fig. 7.

The first row of Fig. 7 shows the thermal distribution evolution of Hankou. Here, it can be seen that the concentrated high temperature zone was slowly scattered and moved to the outskirts of the city over the 26 years. In the latest stage (2008–2013), the old city had almost no significant high temperature zone, except for a belt area. In fact, this belt area is located in the area of the second ring road, where commerce and population are very highly concentrated. Moreover, the area indicated by a circle is a large business zone consisting of a building material market, motor vehicle market, ceramic market, etc. Furthermore, a new high temperature zone (square region) grew up. This is the Linkonggang Economic Development Zone, which is focused on logistics, commerce, and trade.

The thermal distribution evolution of Hanyang is shown in the second row of Fig. 7. Here, the most dramatic change took place in the area indicated by the rectangle, which is the Zhuankou Economic Development Zone. The motor industry and electronics are the two main pillars of industry in this development zone. The rapid industrialization of this region changed the temperature zone from medium and sub-low to high and sub-high. Hanyang had a similar change trend to Hankou, in that the high temperature zone in the old city of Hanyang showed a gradual scattered tendency. In the latest stage (2008–2013), a high temperature belt was still obvious along the main road. The rail transit system under construction was also deemed to contribute to this.

The thermal distribution evolution of Wuchang is shown in the third row of Fig. 7. Again, the high temperature zone clustered in the old city in the early stage, and then scattered as time went on. However, there was one large region which had high temperatures all the time, as labeled by the circle. The reason for this is that this region contains a sizeable iron and steel enterprise, whose output is ranked fifth in the world. The expanded local high temperature zone indicated by the dashed ellipse is also due to the heavy industries, which include a shipyard, glass factory, and carbon black plant. It is worth mentioning that there is a famous development zone in Wuchang, i.e., the East Lake High-tech Development Zone, which is also called Optics Valley of China (indicated by the rectangle). Its main industries include photoelectronics, bioengineering, and geoinformatics. These relatively light industries do not result in high temperatures as much as in the other two large development zones in Hankou and Hanyang.

Fig. 8 (a) shows the distribution of factories in the main city areas, as labeled on a Baidu web map. Although we could not obtain more detailed information, and some of the factories may not have been in production, by a visual comparison with Fig. 8 (b), it is interesting to see that the factory density has a high correlation with the distribution of the high temperature zone. Fig. 8 (b) also shows some of the large commercial districts (circles or ellipses) and residential communities

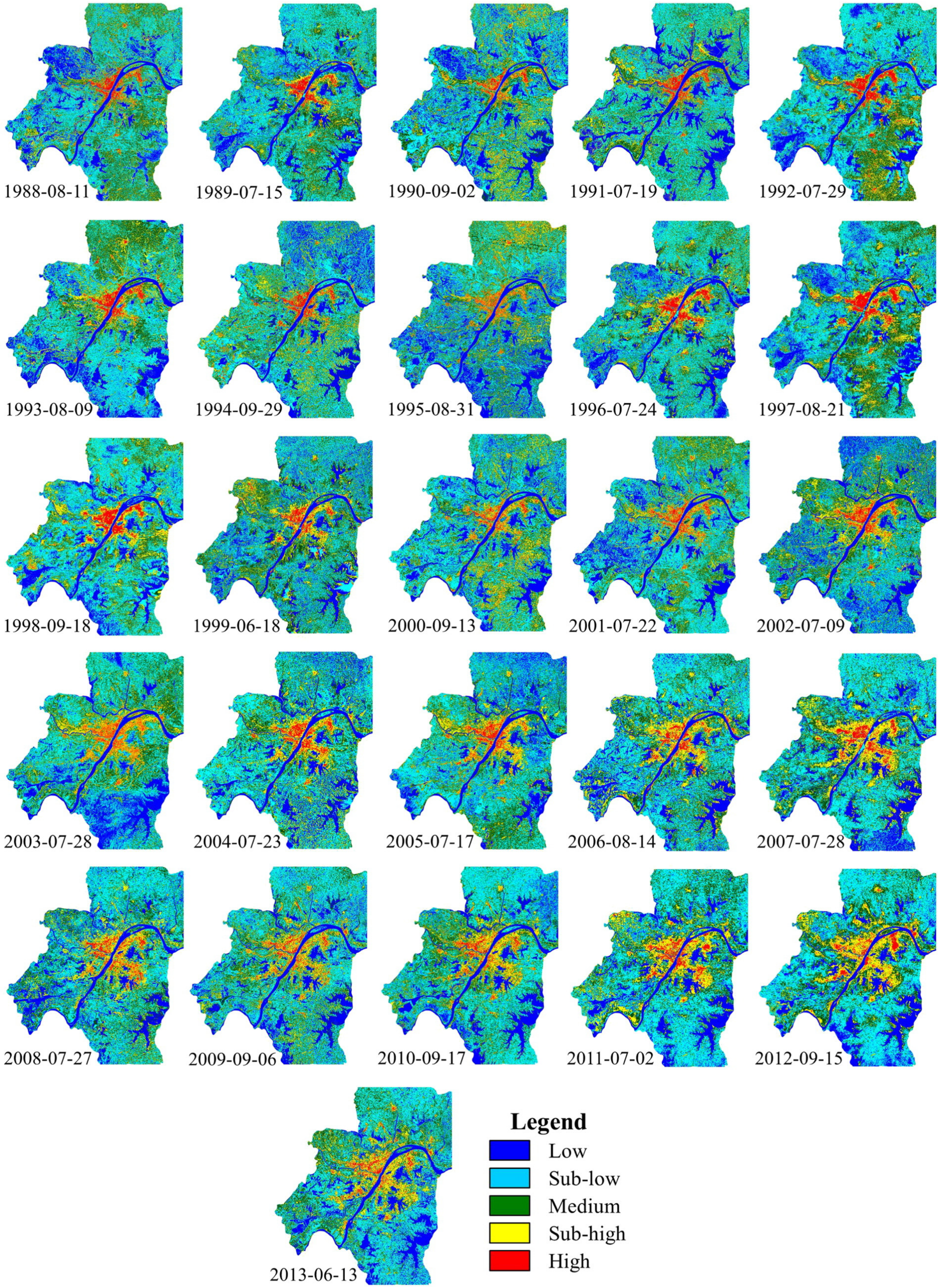

Fig. 5. Summer LST distribution for Wuhan from 1988 to 2013, before the temporal filtering.

(polygons) existing in 2013. Here, it can be seen that there are also high temperature spots in the commercial districts. For the residential communities, although they feature a high population density, the high temperature proportion is not high. This indicates that the influences of industry, businesses, and residential districts on the thermal distribution are in descending order in Wuhan.

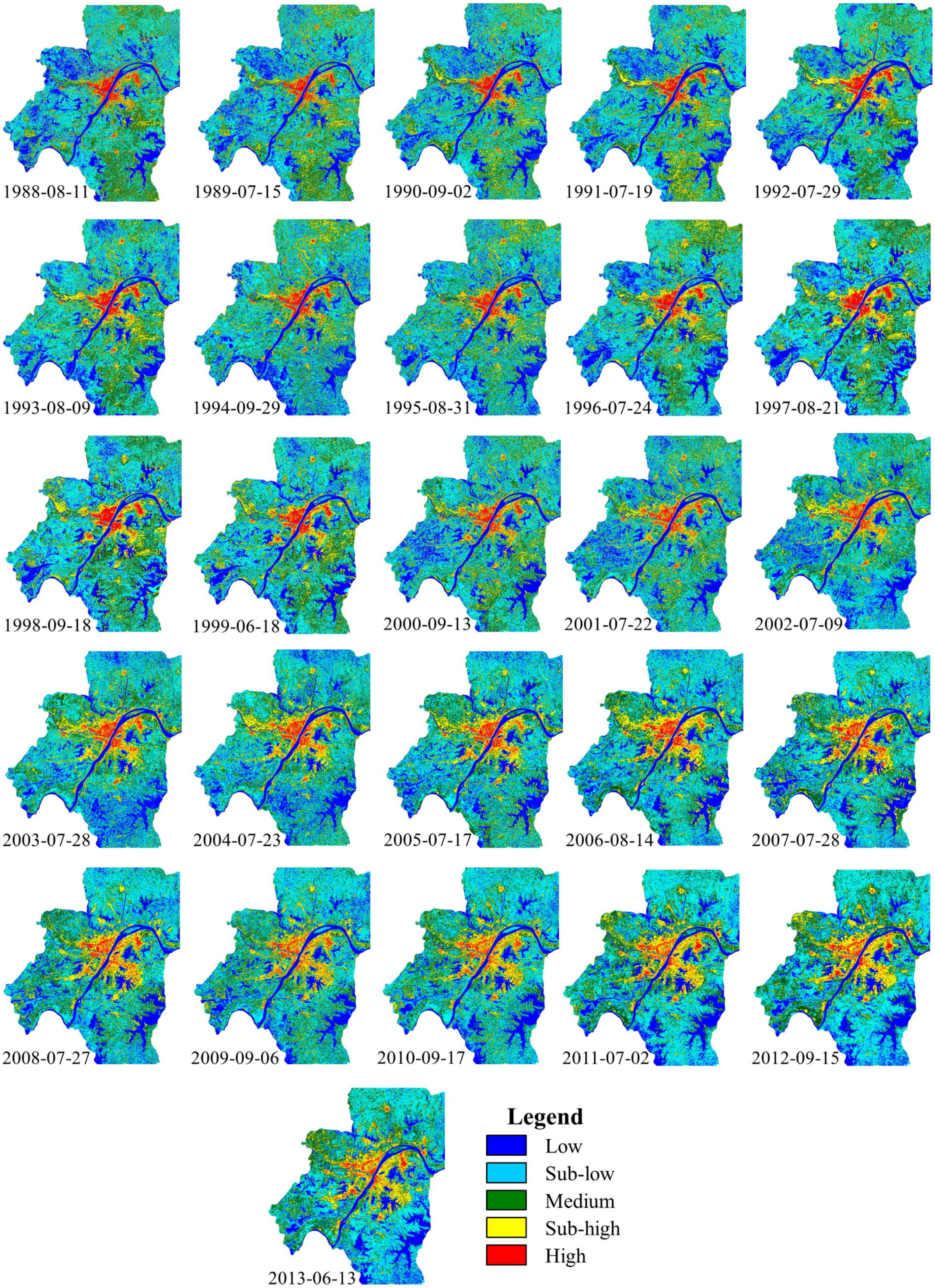

Fig. 6. Summer LST distribution for Wuhan from 1988 to 2013, after the temporal filtering.

In addition to the main city areas, Wuhan also has several outer city zones, such as Huangpi, Yangluo, Jiangxia, Hannan, and Caidian, as shown in Fig. 9. In the past decades, these zones have also developed rapidly, and they have therefore resulted in more and more high temperature and sub-high temperature areas.

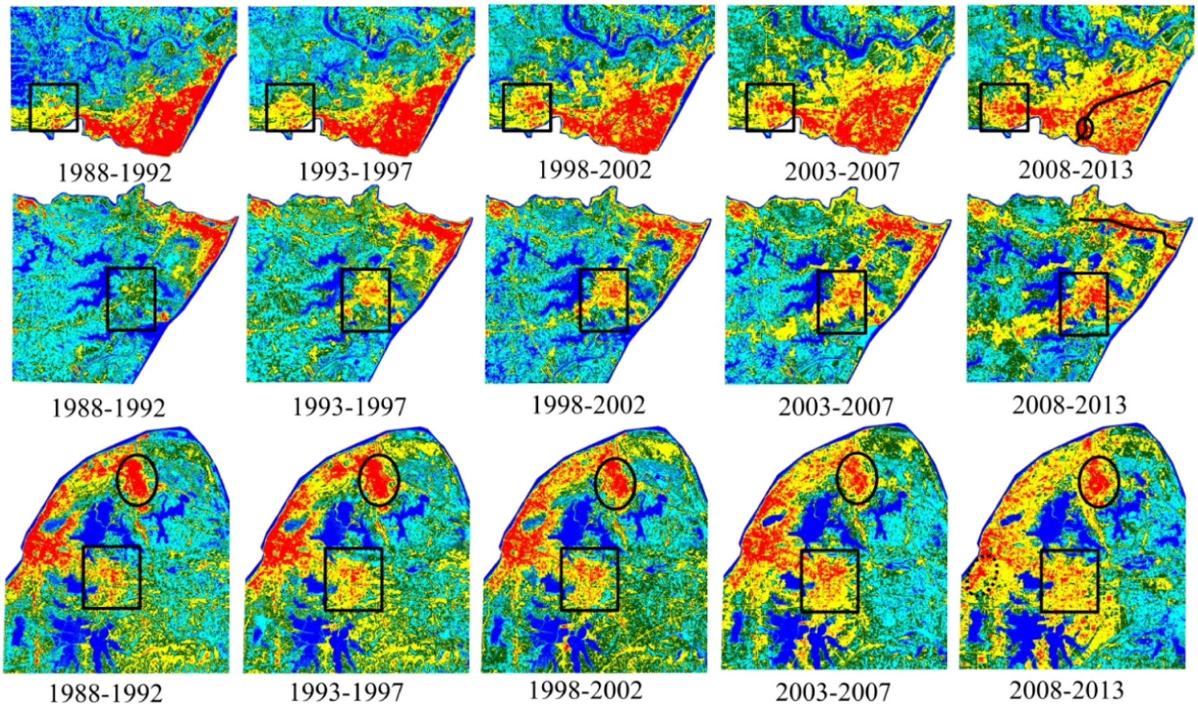

Fig. 7. SUHI patterns of Hankou (the first row), Hanyang (the second row), and Wuchang (the third row) in the five stages, respectively.

3.3. Quantitative evolution analysis of heat aggregation and heat island intensity

A heat aggregation indicator (HAI) based on the RPGS was used to describe the aggregation degree of the high temperature and/or sub-high temperature zones. The HAI counts the area (or pixel number) of the high temperature and/or sub-high temperature zones divided by the RPGS in a region of interest which covers all or part of the urban area. The pixel numbers of high temperature, and high temperature plus sub-high temperature, were respectively counted within the three zones shown in Fig. 10, which are, respectively, the old city zone, the areas within the third ring road, and the areas within the beltway. Among them, the old city zone was delineated from the satellite image of 1988. From Fig. 11, it can be seen that within the beltway area, both the high (Fig. 11 (b)) and high plus sub-high temperature (Fig. 11 (a)) areas showed an increasing tendency on the whole from 1988 to 2013, although there were some fluctuations. Since this region covers most of the urban area, these results demonstrate that the urbanization resulted in the high temperature and sub-high temperature areas being continuously concentrated from rural to urban areas. Within the third ring road area, the high plus sub-high temperature area showed an increasing tendency at first, and then became relatively stable (Fig. 11 (c)) after 2003. At the same time, the high temperature area decreased rapidly after 2003 (Fig. 11 (d)). For the old city zone, the high plus sub-high temperature area increased at first and then later fell, to a small degree, as shown in Fig. 11 (e). Conversely, the high temperature area showed an obvious decrease due to the rapid development of the new city zones and outer city zones (Fig. 11 (f)). In fact, the quantitative analysis of this indicator showed a strong consistency with the evolution process demonstrated in Figs. 6 and 7. The main reason for the HAI change was that the sub-high temperature zone was aggregated to a relatively stable status, and the high temperature zone showed a dispersive tendency, along with the urbanization mode in Wuhan.

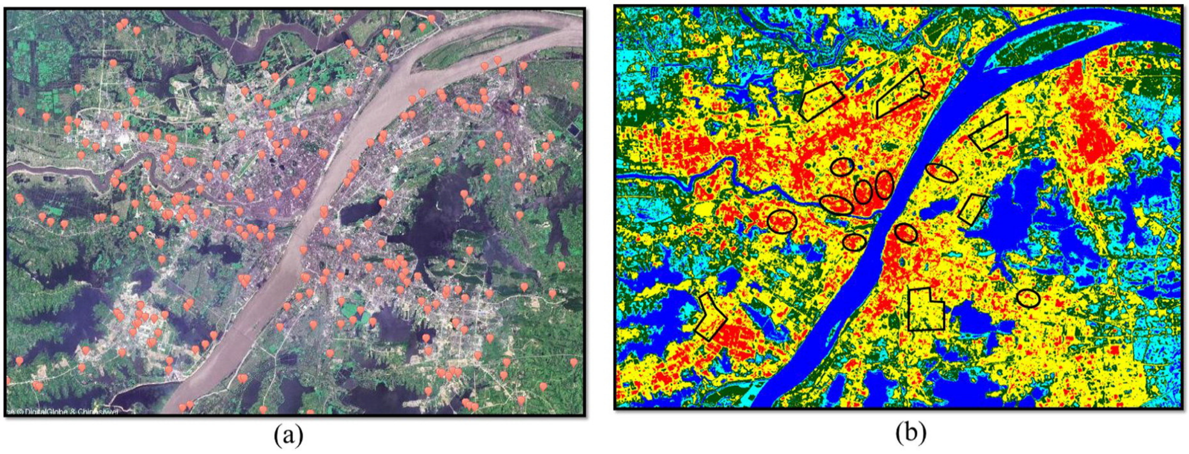
(a)
(b)

Fig. 8. The distribution of factories, businesses, and residential districts. (a) Factories (orange dots) on a Baidu web map. (b) Large business districts (ellipses) and residential communities (polygons) in 2013. (For interpretation of the references to color in this figure legend, the reader is referred to the web version of this article.)

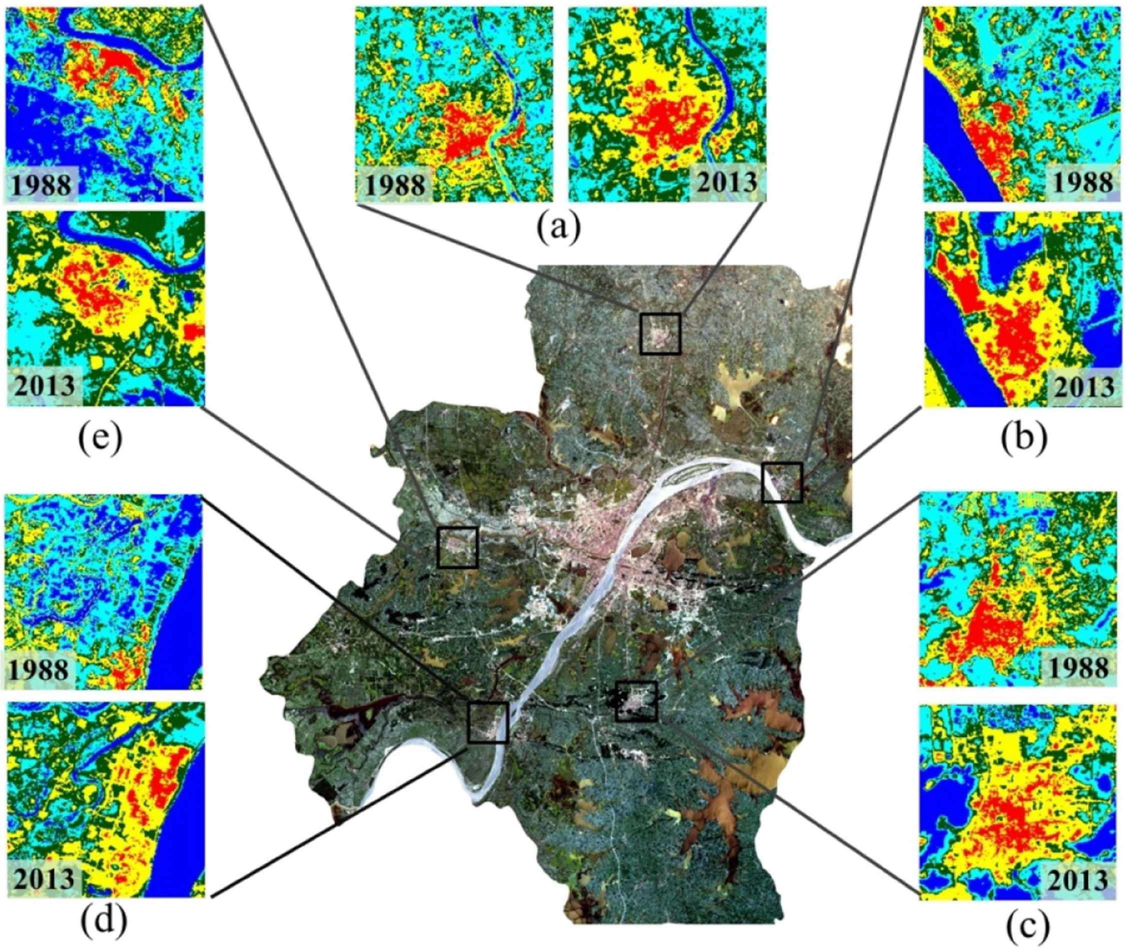

Fig. 9. LSTs of the outer city zones in Wuhan. (a) Huangpi. (b) Yangluo. (c) Jiangxia. (d) Hannan. (e) Caidian.

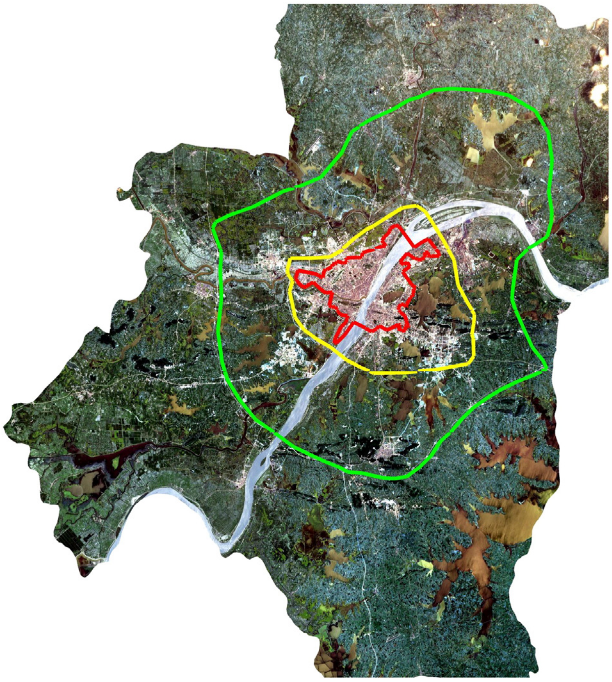

Fig. 10. Areas of interest for quantifying the surface urban heat islands. Rings from inside to outside: the approximate old city border, the third ring road, and the beltway.

In order to quantitatively measure the SUHI effect, the heat island intensity is commonly computed. Although a wide variety of indicators for heat island intensity have been proposed, the temperature difference between urban and rural areas (TDUR) (Gallo et al., 1993; Imhoff et al., 2010; Tomlinson, Chapman, Thornes, & Baker, 2012; Zhou, Rybski, & Kropp, 2013) is the most commonly used indicator. In the literature, the differentiation between "urban" and "rural" remains problematic (Schwarz et al., 2011). For "urban", we respectively chose the old city zone and the area within the third ring road, after removing the water areas. The "rural" category was chosen as all the non-urban and non-water areas. The results are shown in Fig. 12 (a) and (b). Here, it is very interesting that the two figures both show that the SUHI intensity showed a fluctuating increase at first, and then decreased after the peak in 2003. The maximum temperature difference between the old city zone and the rural area was 7.19 K, and the minimum was 4.20 K. The corresponding values for the area within the third ring road were respectively 4.65 K and 2.82 K.

By comparison, we found that the HAI and TDUR showed a strong correlation. A very notable phenomenon was the break point appearing around 2003. For example, the curves in Figs. 11 (d), (f), 12 (a), and (b) begin to drop after 2003, and the curve in Fig. 11 (c) becomes stable from this year. Notably, the phenomenon of the SUHI intensity first increasing and then decreasing has seldom been reported in previous SUHI research. We believe that this evolutionary characteristic in Wuhan can be mainly attributed to the land-cover change caused by the urban development mode. Fig. 13 illustrates the abundance figures for vegetation and impervious surfaces, for 1988, 2003, and 2013,

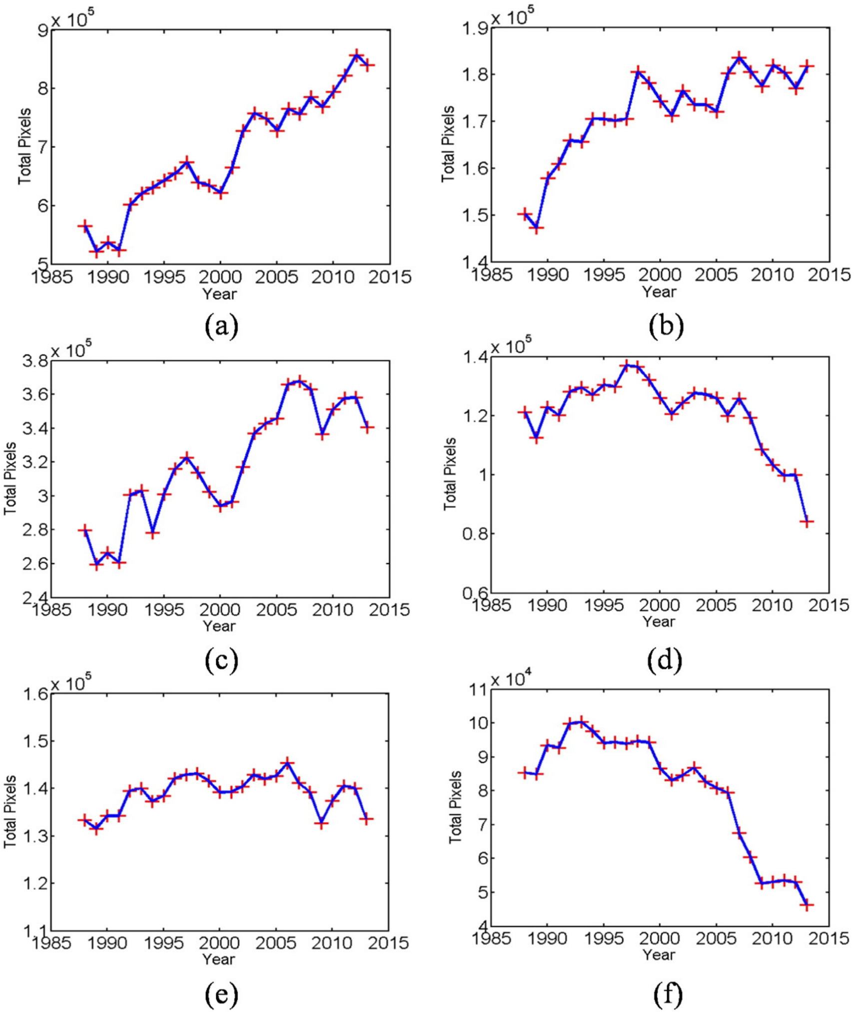

Fig. 11. Heat aggregation indicator (HAI) for Wuhan from 1988 to 2013. (a) High plus sub-high temperature zone within the beltway. (b) High temperature zone within the beltway. (c) High plus sub-high temperature zone within the third ring road. (d) High temperature zone within the third ring road. (e) High plus sub-high temperature zone within the old city zone. (f) High temperature zone within the old city zone.

respectively. The VF and the ISF were determined by a normalized spectral mixture analysis (NSMA) method (Wu, 2004). From 1988 to 2003, the impervious surfaces in the old city zone (delineated by the red line in Fig. 13) increased from 89.21 km^2 to 107.04 km^2, in pace with the urban development. In 2013, this fell back to 97.47 km^2, which was due to community greening, the construction of parks, etc. Conversely, the vegetation area in the old city zone increased after first dropping, being 17.72 km^2, 11.66 km^2, and 25.71 km^2, in 1988, 2003, and 2013, respectively. Moreover, the impervious surfaces in the rural area rapidly increased in the last 10 years, and the corresponding areas were respectively 687.06 km^2 and 1299.69 km^2 in 2003 and 2013.

In the heat island intensity charts, there are also some fluctuations. On the one hand, although the city area always expanded, the urban village renovation resulted in decreased impervious surfaces and increased vegetation in some local areas in the city. On the other hand, in the rural area, the impervious surfaces also showed an increase, and the vegetation decreased. In the past 26 years, Wuhan has undergone

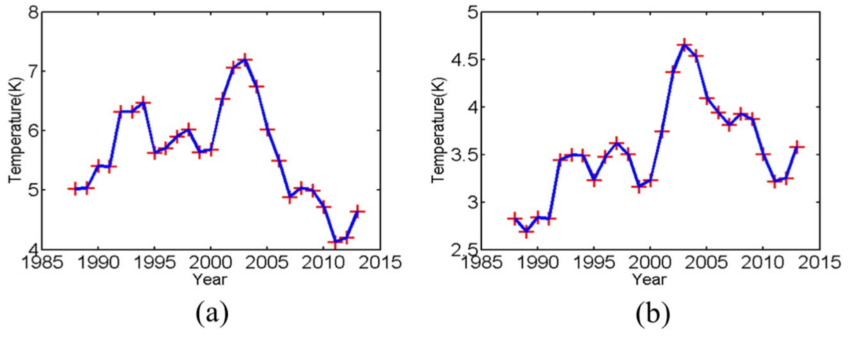

Fig. 12. Heat island intensity in Wuhan from 1988 to 2013. (a) Temperature difference between the old city zone and the rural area. (b) Temperature difference between the urban area within the third ring road and the rural area.

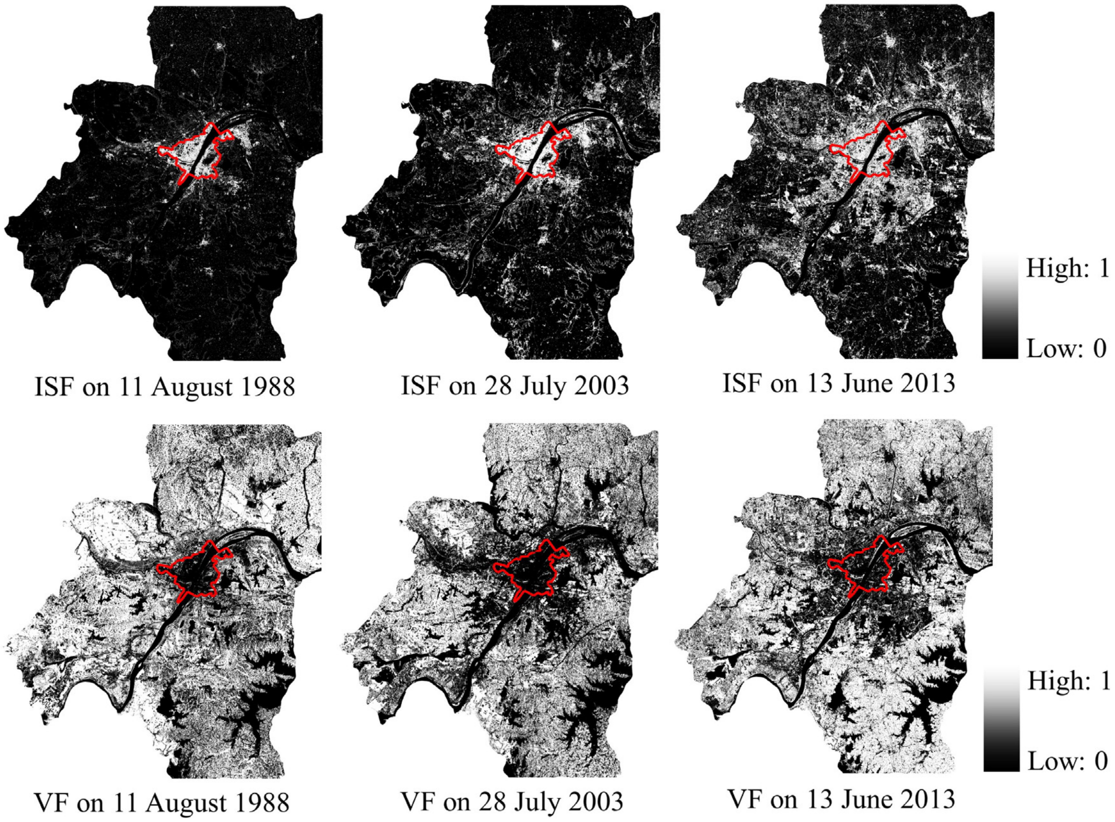

Fig. 13. The impervious surface fraction (ISF) and the vegetation fraction (VF) derived from Landsat images for the study area. The area delineated by the red line represents the old city zone. (For interpretation of the references to color in this figure legend, the reader is referred to the web version of this article.)

dramatic changes, both in the city and in the countryside. The land cover has been influenced by the ongoing urbanization, government policy, and other complicated factors, which resulted in these fluctuations. In the next sub-section, a quantitative analysis is given.

3.4. Spatio-temporal relationship of LST with different indices

It is well known that water, vegetation, and impervious surfaces are very important factors affecting LST distribution in a SUHI analysis. It can be seen from our results that the water bodies in Wuhan had a very obvious cooling effect. However, since the effect of water is embodied by pure pixels, we concentrated on the relationships between LST and vegetation (the NDVI and the VF), as well as LST and impervious surfaces (ISF). It should be noted that the relationships between LST and these indices have been widely researched (Chen et al., 2006; Dousset & Gourmelon, 2003; Li et al., 2011; Yuan & Bauer, 2007). However, these studies were all based on one or a small amount of LST images, because of the lack of available data, and they mainly analyzed the spatial relationship characteristics. Analyses of the temporal changes of these relationships are very limited. To determine the spatio-temporal characteristics of these relationships, we undertook a continuous analysis, based on the fused 26-year data set. In this study, we determined the mean LST at 0.01 intervals for the NDVI and at 1% intervals for the VF and ISF. Considering that the NDVI values of pure bare soil and vegetation are respectively 0.157 and 0.727 (Valor & Caselles, 1996), we computed the relationship between LST and the NDVI only within the interval [0.15, 0.75]. This is a more reasonable approach, as noted by Chen et al. (2006). In order to facilitate the comparison, water bodies were excluded.

The correlation coefficients (R) of LST with the NDVI, the VF, and the ISF are shown in Fig. 14 (a). The mean correlation coefficients for the NDVI, the VF, and the ISF are −0.9752, −0.9642, and 0.8941, respectively. It can also be seen that the fluctuations in the correlation coefficients for the three indices are small. To better understand the relationship characteristics, the spatio-temporal relationships of LST with the NDVI, the VF, and the ISF are illustrated in a three-dimensional mode in Fig. 14 (b), (c), and (d). Here, it is clear that the relationships over the 26 years were fairly stable, although there were some small fluctuations. Comparatively speaking, the fluctuations in the NDVI were greater than in both the VF and ISF. This may be due to the fact that the NDVI is more dependent on the reflectance retrieval. Moreover, it can be seen that the chart of the ISF is more like a curved surface than a planar surface, which demonstrates that this relationship was not strictly linear.

To further investigate these relationships, linear and quadratic functions were respectively fitted and compared. The first row of Fig. 15 shows the regression results between LST and the NDVI, the VF, and the ISF for 2000, 2009, and 2005, respectively. Since the correlation coefficients for these years are the closest to the mean values, we show them as examples. Here, we can see that the quadratic function is more appropriate, especially for the VF and the ISF, and the R^2 values are greatly increased when substituting the linear function with the quadratic function. We also attempted to fit one curve using all the 26-year data. In general, this is very challenging because there can be great inconsistency in long-term data. Nevertheless, the relationships are still oblivious, as shown in the second row of Fig. 15. The correlation coefficients of the NDVI, the VF, and the ISF are respectively −0.9348, −0.9028, and 0.8357. Overall, the difference between the linear and quadratic functions is negligible for the NDVI, but is obvious for the ISF, and the VF lies between the two.

The above two groups of analyses demonstrate that in Wuhan, the NDVI and VF had a strong negative relationship to LST, and the ISF had an obvious positive relationship to LST. In addition, all these relationships were confirmed to be interannually stable. Overall, we believe that the use of the continuous long-term data weakened the interference of poor data quality and improved the reliability.

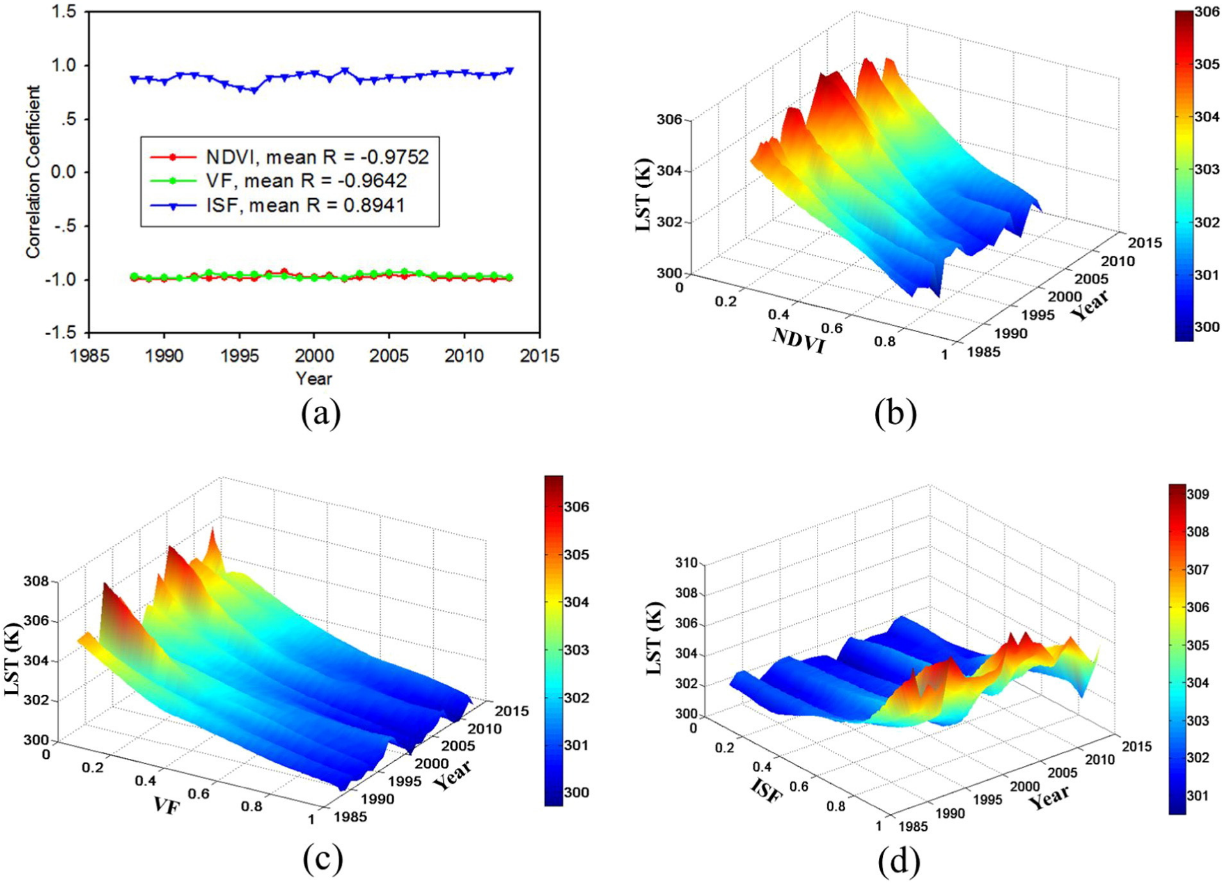

Fig. 14. The spatio-temporal relationships between mean LST and the NDVI, the VF, and the ISF. (a) The correlation coefficients between LST and the NDVI, the VF, and the ISF. (b) The 3D relationship between LST and the NDVI. (c) The 3D relationship between LST and the VF. (d) The 3D relationship between LST and the ISF.

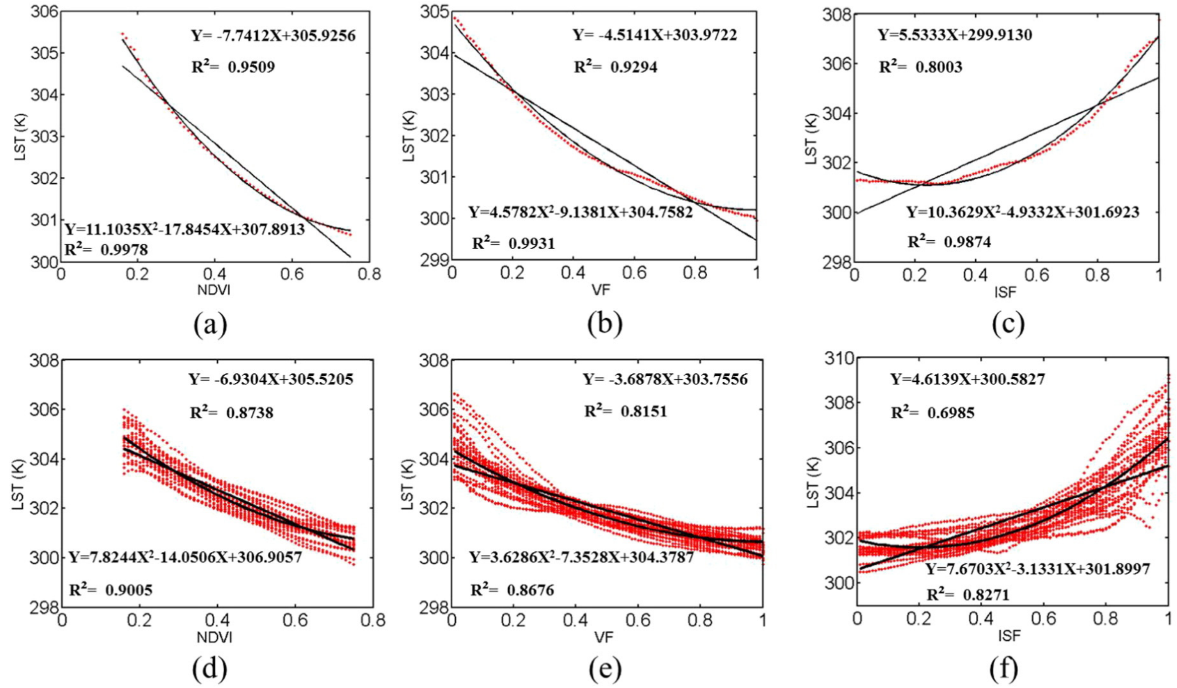

Fig. 15. The first row shows the scatter diagrams and fitted curves of one year's data: (a) LST-NDVI, (b) LST-VF, (c) LST-ISF. The second row shows the scatter diagrams and fitted curves of the 26-year data: (d) LST-NDVI, (e) LST-VF, (f) LST-ISF.

4. Discussion and conclusions

The trade-off between the spatial and temporal resolutions is the main restraining factor in SUHI research. This study has demonstrated the feasibility of employing data fusion methods for long-term and fine-scale SUHI analysis. Through the multi-temporal and multi-sensor fusion of TM, ETM+, OLI, TIRS, MODIS, and AVHRR data, a series of 26-year LSTs were generated for the city of Wuhan in China. Based on this data set, a long-term analysis at the Landsat scale was undertaken. It was found that the use of the continuous long-term data produced by the fusion methods is able to weaken the interference of poor data quality and can enhance the understanding of SUHI growth and its evolution mechanism.

Using the continuous 26-year data, we have provided a clear picture of the spatio-temporal changes in heat distribution and aggregation. On the one hand, along with the urbanization of Wuhan, the higher temperatures (high and sub-high temperature zones) were continuously concentrated from rural to urban areas from 1988 to 2013. In the central part of Wuhan, a wide range of obvious heat island structures were formed. On the other hand, the highest temperatures had a tendency to transfer from the old city zone to the newly established development zones, resulting in the high temperature zone becoming more and more scattered, which is a very interesting phenomenon.

Secondly, using the classic TDUR indicator, we observed an important characteristic of the SUHI intensity. In general, the SUHI intensity first increased and then decreased over the 26 years. For the old city zone, the maximum temperature difference between the city zone and the rural area was 7.19 K, and the minimum was 4.20 K. The corresponding values for the area within the third ring road were respectively 4.65 K and 2.82 K. For both areas, the peak arose in 2003.

Thirdly, we have provided new insights into the relationships between heat distribution and the NDVI, VF, and ISF indices. Our results indicated that these relationships were interannually stable. The average correlation coefficients for the NDVI, VF, and ISF indices and heat distribution were −0.9752, −0.9642, and 0.8941, respectively. Furthermore, we also found that the relationships were not truly linear, and the R^2 can be considerably improved when using a quadratic function. This result agrees with the results in the research of Chen et al. (2006) and Xian (2008).

We next discuss some possible uncertainties inherent in this research. The first uncertainty is with regard to the multi-temporal fusion method, the accuracy of which can be influenced by vegetation phenology. In general, the closer the dates of the two images, the better the reconstruction. However, we found that the influence of vegetation phenology was not significant for the LST retrieval in this research, which was verified in the quantitative evaluation in Section 3.1. When the two images were acquired, respectively, in March and July, the error was only about 1 K, which satisfies our application requirements. Furthermore, for fractus cloud removal, the restored LST is actually the value under clear sky conditions, which may be higher than the value for the actual cloudy conditions. However, we believe that this should not affect the applicability, because in the long time series analysis of the SUHI effect, only the cloudless LST can reflect real SUHI changes.

Moreover, the multi-sensor fusion accuracy can be affected by several factors. For example, the difference in viewing angles of MODIS and AVHRR can lead to considerable uncertainties. To deal with this problem, we selected images with similar viewing angles; otherwise, angle correction would have been required. Another notable point is that the acquisition times of the known low-resolution and high-resolution pair should not have a great difference. It was also noted in Section 2.5 that special attention should be paid to the fusion of Landsat and AVHRR data. Finally, the multi-sensor fusion method was originally used for reflectance data, and considerable errors can be produced when the land cover changes. However, we found that this problem was greatly alleviated when the multi-sensor fusion method was used for the LST fusion. The main reason for this may be that the LST product is much smoother than the reflectance product in spatial structure.

How to make the years of LST data comparable is another important issue in SUHI evolution research. Although the temporal aggregation products have been widely used for representing an annual normal condition, Hu and Brunsell (2013) proved that they can result in a loss of accuracy, particularly for summer daytime data. In our research, we were mainly concerned with how the high and sub-high LSTs transferred and aggregated along with the urbanization of Wuhan. Thus, the temporal aggregation method may have led to unacceptable errors in this study. Therefore, we selected a high-quality and high-resolution LST product for each year by directs retrieval or data fusion. In order to improve the comparability, a moment matching method was employed to normalize the LSTs in the different years. After this normalization, the comparability was greatly improved. Furthermore, since we were mainly concerned with the overall tendency of the 26 years, a one-dimension low-pass temporal filtering was also performed on the LSTs to further relieve any possible uncertainties.

In summary, although there are some uncertainties in the technical framework, they can be controlled by adopting appropriate countermeasures. Therefore, this research could be used to guide further studies in applying the framework to other regions and making more comprehensive analyses with the auxiliary of different types of data. Nevertheless, some aspects deserve further investigation, such as the consideration of temperature cycles and urban thermal landscape heterogeneity (Weng et al., 2014). Furthermore, the SUHI effect changes along with the seasons and also diurnally, and research into this aspect coupled with air temperature measurements is worthy of further investigation. Finally, Wuhan is regarded as one of the hottest “stove cities” in China. How to mitigate or minimize the UHI effect will therefore be a very significant topic for future research.

Acknowledgments

This research was supported by the Major State Basic Research Development Program (2011CB707103) and the National Natural Science Foundation of China (41422108, 41271376, 41501376). We would also like to thank the data providers of USGS's Earth Resources Observation and Science (EROS) Center, NOAA's Comprehensive Large Array-data Stewardship System (CLASS), and NASA's Level 1 and Atmosphere Archive and Distribution System (LAADS).

References

Adler-Golden, S.M., Matthew, M.W., Bernstein, L.S., Levine, R.Y., Berk, A., Richtsmeier, S.C., ... Gardner, J. (1999). Atmospheric correction for shortwave spectral imagery based on MODTRAN4. *SPIE's International Symposium on Optical Science, Engineering, and Instrumentation* (pp. 61–69). International Society for Optics and Photonics.

Aniello, C., Morgan, K., Busbey, A., & Newland, L. (1995). Mapping micro-urban heat islands using Landsat TM and a GIS. *Computers & Geosciences*, *21*, 965–969.

Artis, D.A., & Carnahan, W.H. (1982). Survey of emissivity variability in thermography of urban areas. *Remote Sensing of Environment*, *12*, 313–329.

Cai, G., Du, M., & Xue, Y. (2011). Monitoring of urban heat island effect in Beijing combining ASTER and TM data. *International Journal of Remote Sensing*, *32*, 1213–1232.

Chander, G., Markham, B.L., & Helder, D.L. (2009). Summary of current radiometric calibration coefficients for Landsat MSS, TM, ETM+, and EO-1 ALI sensors. *Remote Sensing of Environment*, *113*, 893–903.

Chen, X. -L., Zhao, H. -M., Li, P. -X., & Yin, Z. -Y. (2006). Remote sensing image-based analysis of the relationship between urban heat island and land use/cover changes. *Remote Sensing of Environment*, *104*, 133–146.

Cui, Y.Y., & De Foy, B. (2012). Seasonal variations of the urban heat island at the surface and the near-surface and reductions due to urban vegetation in Mexico City. *Journal of Applied Meteorology and Climatology*, *51*, 855–868.

DESA, U. (2002). World urbanization prospects: The 2001 revision, data tables and highlights. *United Nations Population Division—Department of Economic and Social Affairs, United Nations Secretariat (ESA/P/WP. 173), New York* (Available at: www.un.org/esa/population/publications/wup2001/wup2001dh.pdf).

Dixon, P.G., & Mote, T.L. (2003). Patterns and causes of Atlanta's urban heat island-initiated precipitation. *Journal of Applied Meteorology*, *42*, 1273–1284.

Dousset, B., & Gourmelon, F. (2003). Satellite multi-sensor data analysis of urban surface temperatures and landcover. *ISPRS Journal of Photogrammetry and Remote Sensing*, *58*, 43–54.

Gadallah, F., Csillag, F., & Smith, E. (2000). Destriping multisensor imagery with moment matching. *International Journal of Remote Sensing*, *21*, 2505–2511.

Gallo, K., McNab, A., Karl, T., Brown, J., Hood, J., & Tarpley, J. (1993). The use of NOAA AVHRR data for assessment of the urban heat island effect. *Journal of Applied Meteorology*, *32*, 899–908.

Gao, F., Masek, J., Schwaller, M., & Hall, F. (2006). On the blending of the Landsat and MODIS surface reflectance: Predicting daily Landsat surface reflectance. *IEEE Trans. Geosci. Remote Sens.*, *44*, 2207–2218.

Grimm, N.B., Faeth, S.H., Golubiewski, N.E., Redman, C.L., Wu, J., Bai, X., & Briggs, J.M. (2008). Global change and the ecology of cities. *Science*, *319*, 756–760.

Han, Y., Li, S., & Zheng, Y. (2009). Predictors of nutritional status among community-dwelling older adults in Wuhan, China. *Public Health Nutrition*, *12*, 1189–1196.

Harlan, S.L., Brazel, A.J., Prashad, L., Stefanov, W.L., & Larsen, L. (2006). Neighborhood microclimates and vulnerability to heat stress. *Social Science & Medicine*, *63*, 2847–2863.

Hilker, T., Wulder, M.A., Coops, N.C., Seitz, N., White, J.C., Gao, F., ... Stenhouse, G. (2009). Generation of dense time series synthetic Landsat data through data blending with MODIS using a spatial and temporal adaptive reflectance fusion model. *Remote Sensing of Environment*, *113*, 1988–1999.

Hu, L., & Brunsell, N.A. (2013). The impact of temporal aggregation of land surface temperature data for surface urban heat island (SUHI) monitoring. *Remote Sensing of Environment*, *134*, 162–174.

Imhoff, M.L., Zhang, P., Wolfe, R.E., & Bounoua, L. (2010). Remote sensing of the urban heat island effect across biomes in the continental USA. *Remote Sensing of Environment*, *114*, 504–513.

Jiménez-Muñoz, J.C., & Sobrino, J.A. (2003). A generalized single-channel method for retrieving land surface temperature from remote sensing data. *Journal of Geophysical Research – Atmospheres (1984–2012)*, *108*.

Kalnay, E., & Cai, M. (2003). Impact of urbanization and land-use change on climate. *Nature*, *423*, 528–531.

Knapp, S., Kühn, I., Stolle, J., & Klotz, S. (2010). Changes in the functional composition of a Central European urban flora over three centuries. *Perspectives in Plant Ecology, Evolution and Systematics*, *12*, 235–244.

Kuttler, W., Weber, S., Schonnefeld, J., & Hesselschwerdt, A. (2007). Urban/rural atmospheric water vapour pressure differences and urban moisture excess in Krefeld, Germany. *International Journal of Climatology*, *27*, 2005–2015.

Lafortezza, R., Carrus, G., Sanesi, G., & Davies, C. (2009). Benefits and well-being perceived by people visiting green spaces in periods of heat stress. *Urban Forestry & Urban Greening*, *8*, 97–108.

Li, J. -j., Wang, X. -r., Wang, X. -j., Ma, W. -c., & Zhang, H. (2009). Remote sensing evaluation of urban heat island and its spatial pattern of the Shanghai metropolitan area, China. *Ecological Complexity*, *6*, 413–420.

Li, J., Song, C., Cao, L., Zhu, F., Meng, X., & Wu, J. (2011). Impacts of landscape structure on surface urban heat islands: A case study of Shanghai, China. *Remote Sensing of Environment*, *115*, 3249–3263.

Li, Y. -y., Zhang, H., & Kainz, W. (2012). Monitoring patterns of urban heat islands of the fast-growing Shanghai metropolis, China: Using time-series of Landsat TM/ETM+ data. *International Journal of Applied Earth Observation and Geoinformation*, *19*, 127–138.

Li, X., Zhou, W., & Ouyang, Z. (2013). Relationship between land surface temperature and spatial pattern of greenspace: What are the effects of spatial resolution? *Landscape and Urban Planning*, *114*, 1–8.

Lo, C., & Quattrochi, D.A. (2003). Land-use and land-cover change, urban heat island phenomenon, and health implications. *Photogrammetric Engineering & Remote Sensing*, *69*, 1053–1063.

Mackey, C.W., Lee, X., & Smith, R.B. (2012). Remotely sensing the cooling effects of city scale efforts to reduce urban heat island. *Building and Environment*, *49*, 348–358.

Masek, J.G., Vermote, E.F., Saleous, N.E., Wolfe, R., Hall, F.G., Huemmrich, K.F., ... Lim, T. -K. (2006). A Landsat surface reflectance dataset for North America, 1990–2000. *IEEE Geosci. Remote Sens. Lett.*, *3*, 68–72.

Meng, J., Du, X., & Wu, B. (2013). Generation of high spatial and temporal resolution NDVI and its application in crop biomass estimation. *International Journal of Digital Earth*, *6*, 203–218.

Oke, T.R. (1982). The energetic basis of the urban heat island. *Quarterly Journal of the Royal Meteorological Society*, *108*, 1–24.

Qian, Z., He, Q., Lin, H. -M., Kong, L., Liao, D., Dan, J., ... Wang, B. (2007). Association of daily cause-specific mortality with ambient particle air pollution in Wuhan, China. *Environmental Research*, *105*, 380–389.

Qin, Z. -h., Karnieli, A., & Berliner, P. (2001). A mono-window algorithm for retrieving land surface temperature from Landsat TM data and its application to the Israel–Egypt border region. *International Journal of Remote Sensing*, *22*, 3719–3746.

Quan, J., Chen, Y., Zhan, W., Wang, J., Voogt, J., & Wang, M. (2014). Multi-temporal trajectory of the urban heat island centroid in Beijing, China based on a Gaussian volume model. *Remote Sensing of Environment*, *149*, 33–46.

Rajasekar, U., & Weng, Q. (2009a). Spatio-temporal modelling and analysis of urban heat islands by using Landsat TM and ETM+ imagery. *International Journal of Remote Sensing*, *30*, 3531–3548.

Rajasekar, U., & Weng, Q. (2009b). Urban heat island monitoring and analysis using a non-parametric model: A case study of Indianapolis. *ISPRS Journal of Photogrammetry and Remote Sensing*, *64*, 86–96.

Ruppert, D., & Wand, M.P. (1994). Multivariate locally weighted least squares regression. *The Annals of Statistics*, 1346–1370.

Schwarz, N., Lautenbach, S., & Seppelt, R. (2011). Exploring indicators for quantifying surface urban heat islands of European cities with MODIS land surface temperatures. *Remote Sensing of Environment*, *115*, 3175–3186.

Shen, H., Wu, P., Liu, Y., Ai, T., Wang, Y., & Liu, X. (2013). A spatial and temporal reflectance fusion model considering sensor observation differences. *International Journal of Remote Sensing*, *34*, 4367–4383.

Shen, H., Jiang, W., Zhang, H., & Zhang, L. (2014). A piece-wise approach to removing the nonlinear and irregular stripes in MODIS data. *International Journal of Remote Sensing*, *35*, 44–53.

Sisterson, D.L., & Dirks, R.A. (1967). (1978). Structure of the daytime urban moisture field. *Atmospheric Environment*, *12*, 1943–1949.

Sobrino, J.A., Jiménez-Muñoz, J.C., & Paolini, L. (2004). Land surface temperature retrieval from LANDSAT TM 5. *Remote Sensing of Environment*, *90*, 434–440.

Sobrino, J., Oltra-Carrió, R., Sòria, G., Bianchi, R., & Paganini, M. (2012). Impact of spatial resolution and satellite overpass time on evaluation of the surface urban heat island effects. *Remote Sensing of Environment*, *117*, 50–56.

Steeneveld, G., Koopmans, S., Heusinkveld, B., Van Hove, L., & Holtslag, A. (2011). Quantifying urban heat island effects and human comfort for cities of variable size and urban morphology in The Netherlands. *Journal of Geophysical Research: Atmospheres (1984–2012)*, *116*.

Streutker, D.R. (2002). A remote sensing study of the urban heat island of Houston, Texas. *International Journal of Remote Sensing*, *23*, 2595–2608.

Streutker, D.R. (2003). Satellite-measured growth of the urban heat island of Houston, Texas. *Remote Sensing of Environment*, *85*, 282–289.

Su, W., Gu, C., & Yang, G. (2010). Assessing the impact of land use/land cover on urban heat island pattern in Nanjing City, China. *Journal of Urban Planning and Development*, *136*, 365–372.

Tapper, N. (1990). Urban influences on boundary layer temperature and humidity: Results from Christchurch, New Zealand. *Atmospheric Environment Part B Urban Atmosphere*, *24*, 19–27.

Tomlinson, C., Chapman, L., Thornes, J., & Baker, C. (2012). Derivation of Birmingham's summer surface urban heat island from MODIS satellite images. *International Journal of Climatology*, *32*, 214–224.

Valor, E., & Caselles, V. (1996). Mapping land surface emissivity from NDVI: Application to European, African, and South American areas. *Remote Sensing of Environment*, *57*, 167–184.

Van de Griend, A., & Owe, M. (1993). On the relationship between thermal emissivity and the normalized difference vegetation index for natural surfaces. *International Journal of Remote Sensing*, *14*, 1119–1131.

Voogt, J.A., & Oke, T.R. (2003). Thermal remote sensing of urban climates. *Remote Sensing of Environment*, *86*, 370–384.

Wan, Z., Zhang, Y., Zhang, Q., & Li, Z. -L. (2004). Quality assessment and validation of the MODIS global land surface temperature. *International Journal of Remote Sensing*, *25*, 261–274.

Wang, K., Wang, J., Wang, P., Sparrow, M., Yang, J., & Chen, H. (2007). Influences of urbanization on surface characteristics as derived from the moderate-resolution imaging spectroradiometer: A case study for the Beijing metropolitan area. *Journal of Geophysical Research: Atmospheres (1984–2012)*, *112*.

Weng, Q. (2003). Fractal analysis of satellite-detected urban heat island effect. *Photogrammetric Engineering & Remote Sensing*, *69*, 555–566.

Weng, Q., Lu, D., & Schubring, J. (2004). Estimation of land surface temperature–vegetation abundance relationship for urban heat island studies. *Remote Sensing of Environment*, *89*, 467–483.

Weng, Q., Fu, P., & Gao, F. (2014). Generating daily land surface temperature at Landsat resolution by fusing Landsat and MODIS data. *Remote Sensing of Environment*, *145*, 55–67.

Wu, C. (2004). Normalized spectral mixture analysis for monitoring urban composition using ETM+ imagery. *Remote Sensing of Environment*, *93*, 480–492.

Wu, P., Shen, H., Ai, T., & Liu, Y. (2013). Land-surface temperature retrieval at high spatial and temporal resolutions based on multi-sensor fusion. *International Journal of Digital Earth*, *6*, 113–133.

Xian, G. (2008). Satellite remotely-sensed land surface parameters and their climatic effects for three metropolitan regions. *Advances in Space Research*, *41*, 1861–1869.

Xie, Q., Zhou, Z., Teng, M., & Wang, P. (2012). A multi-temporal Landsat TM data analysis of the impact of land use and land cover changes on the urban heat island effect. *Journal of Food, Agriculture and Environment*, *10*, 803–809.

Yuan, F., & Bauer, M.E. (2007). Comparison of impervious surface area and normalized difference vegetation index as indicators of surface urban heat island effects in Landsat imagery. *Remote Sensing of Environment*, *106*, 375–386.

Zeng, C., Shen, H., & Zhang, L. (2013). Recovering missing pixels for Landsat ETM+ SLC-off imagery using multi-temporal regression analysis and a regularization method. *Remote Sensing of Environment*, *131*, 182–194.

Zhang, J., & Wang, Y. (2008). Study of the relationships between the spatial extent of surface urban heat islands and urban characteristic factors based on Landsat ETM+ data. *Sensors*, *8*, 7453–7468.

Zhang, H., Qi, Z. -f., Ye, X. -y., Cai, Y. -b., Ma, W. -c., & Chen, M. -n. (2013). Analysis of land use/land cover change, population shift, and their effects on spatiotemporal patterns of urban heat islands in metropolitan Shanghai, China. *Applied Geography*, *44*, 121–133.

Zhou, W., Huang, G., & Cadenasso, M.L. (2011). Does spatial configuration matter? Understanding the effects of land cover pattern on land surface temperature in urban landscapes. *Landscape and Urban Planning*, *102*, 54–63.

Zhou, B., Rybski, D., & Kropp, J.P. (2013). On the statistics of urban heat island intensity. *Geophysical Research Letters*, *40*, 5486–5491.